



Review

Power Converter Solutions for Industrial PV Applications—A Review

Ievgen Verbytskyi ¹, Mykola Lukianov ¹, Kawsar Nassereddine ^{2,*}, Bohdan Pakhaliuk ³, Oleksandr Husev ^{4,*} and Ryszard Michał Strzelecki ³

¹ Igor Sikorsky Kyiv Polytechnic Institute, National Technical University of Ukraine, 03056 Kyiv, Ukraine; verbytskyi.ievgen@gmail.com (I.V.); zebrahead097@gmail.com (M.L.)

² Faculty of Engineering, Lebanese University, Beirut 1002, Lebanon

³ Department of Power Electronics and Electrical Machines, Faculty of Electrical and Control Engineering, Gdańsk University of Technology, 80-233 Gdansk, Poland; bohdan.pakhaliuk@pg.edu.pl (B.P.); ryszard.strzelecki@pg.edu.pl (R.M.S.)

⁴ Department of Electrical Power Engineering and Mechatronics, Tallinn University of Technology, 19086 Tallinn, Estonia

* Correspondence: nassereddinejana@gmail.com (K.N.); oleksandr.husev@taltech.ee (O.H.)

Abstract: As the use of photovoltaics becomes more widespread, new technologies for more efficient energy generation, transmission, and distribution based on power electronics converters are being developed. The most common applications are grid-on, energy storage, hybrid, and high voltage gain applications. These applications impose several additional requirements in the design of power converters associated with the solar battery's maximum power tracking and operation in a wide range of input currents and voltages. The practical realization of such solutions can be implemented on the basis of various topologies, which requires a preliminary application of criteria for assessing their effectiveness. The paper conducts a comparison of different topologies on power converters based on two parameters that describe their cost and power loss for various PV applications. For a straightforward study, these parameters are represented using the gain factor, which allows for an accurate comparison of the efficiency of various types of converters.

Keywords: power converters; PV applications review; cost factor; power loss



Citation: Verbytskyi, I.; Lukianov, M.; Nassereddine, K.; Pakhaliuk, B.; Husev, O.; Strzelecki, R.M. Power Converter Solutions for Industrial PV Applications—A Review. *Energies* **2022**, *15*, 3295. <https://doi.org/10.3390/en15093295>

Academic Editors: Diego Bellan and Jelena Loncarski

Received: 4 April 2022

Accepted: 28 April 2022

Published: 30 April 2022

Publisher's Note: MDPI stays neutral with regard to jurisdictional claims in published maps and institutional affiliations.



Copyright: © 2022 by the authors. Licensee MDPI, Basel, Switzerland. This article is an open access article distributed under the terms and conditions of the Creative Commons Attribution (CC BY) license (<https://creativecommons.org/licenses/by/4.0/>).

1. Introduction

The modern development of the energy industry implies a gradual abandonment of fossil energy sources and a transition to renewable energy, i.e., solar, wind, geothermal, hydro energy, and biofuels [1]. Wind power plants currently produce 52% of total electricity generated from renewable sources (excluding hydropower), while solar power plants produce 26% [2]. Solar power plants, on the other hand, rank first in terms of installed capacity for 2020, with 125 GW compared to 110 GW for wind power plants. There are cheaper materials for solar panels, such as silicon [3], and it costs less to keep them up and running [4].

The main economic constraint on the use of solar power plants, namely the higher cost of electricity than for fossil energy sources, is gradually being eliminated. However, solar energy loses in terms of technical indicators: specific capacity, generation stability, cost of maintenance, and infrastructure, which is the main deterrent to its rapid spread [5,6]. So, to overcome this gap, it is necessary to modernize power plant infrastructure. Among these actions, here are the ones that should be highlighted [7]:

- Maximum power point tracking;
- Energy storage and balancing;
- Electric parameter transformation and stabilization.

The generation of solar battery power is characterized by a family of power curves for different solar insolation powers: P_{SI1} , P_{SI2} , and P_{SI3} as functions of voltage U , $P = f(U)$, or current I , $P = f(I)$, as shown in Figure 1a,b. A high level of efficiency is reached when the solar battery is near the maximum power point (MPP) [8], where $P_{MPP} = f(U_{MPP})$ or $P_{MPP} = f(I_{MPP})$ with power from the solar panel 1, 2, and 3.

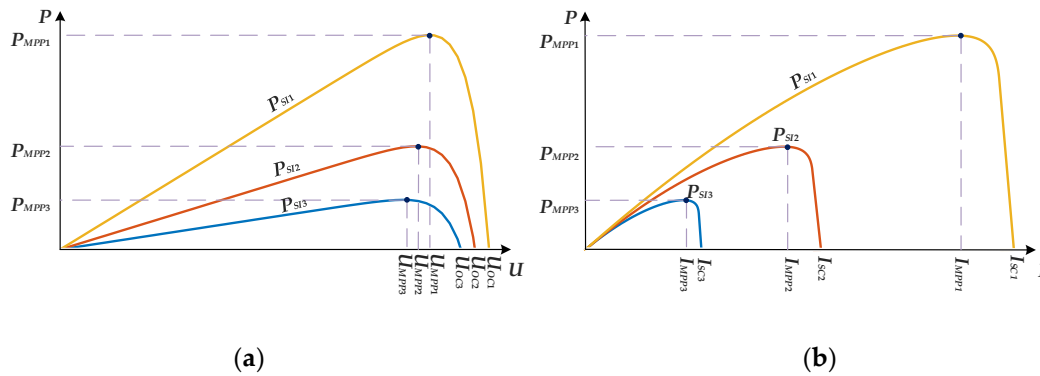


Figure 1. A family of power curves for different solar insolation powers: (a) as functions of voltage U , $P = f(U)$; (b) as functions of current I , $P = f(I)$.

For voltage curves, MPP coordinates U_{MPP} are defined by the open circuit solar battery voltage U_{OC} which is almost constant and belongs to the narrow range $U_{MPP} \in [0.72 \cdot U_{OC}; 0.76 \cdot U_{OC}]$ that slightly depends on solar insolation power P_{SI} . The current MPP co-ordinate I_{MPP} is influenced by the short-circuit current I_{SC} , $I_{MPP} \in [0.9 \cdot I_{SC}; 0.93 \cdot I_{SC}]$. However, the short-circuit current, I_{SC} , in contrast to the open-circuit voltage, varies widely and is proportional to P_{SI} [9].

If a load with resistance R_L is connected directly to a solar battery, maximum power P_{MPP} is delivered to the load when the equivalent resistance of the solar battery R_{SB} is equal to the load resistance R_L in MPT:

$$R_{SB} = \frac{U_{MPP}}{I_{MPP}} = R_L, \tag{1}$$

in another case, when $R_{SB} \neq R_L$, power converters as maximum power point trackers (MPPT) are used [10]. The power converter via output voltage (current) U_L (I_L) regulation tunes equivalent load resistance $R_{L(eq)}$ on the converter primary side according to Equation (2) as shown in Figure 2:

$$R_{SB} = R_{L(eq)} = \frac{U_{MPP}}{I_{MPP}} = \frac{U_L}{G} \cdot \frac{1}{I_L G} = \frac{R_L}{G^2}, \tag{2}$$

where G is a converter voltage gain.

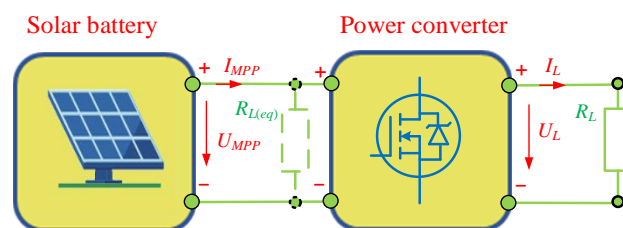


Figure 2. Equivalent load resistance $R_{L(eq)}$ tuning with a power converter.

However, even a power converter such as MPPT does not always provide an efficient mode of solar battery operation. As shown in Figure 3a, only constant solar battery current I_{MPT} that fits MPP allows for generating of maximum power for defined solar insolation P_{SI} . If the solar battery current has ripple ΔI , output power pulsation ΔP appears and decreases

average power P proportionally to ripple amplitude ΔI as shown in Figure 3b [11]. If the input current is discontinuous, then solar battery energy is used inefficiently as shown in Figure 3c. Therefore, the aforementioned features of the solar batteries impose additional requirements on the power converter as an MPPT, specifically:

- Continuous low ripple input current I ;
- High efficiency in a wide power range.

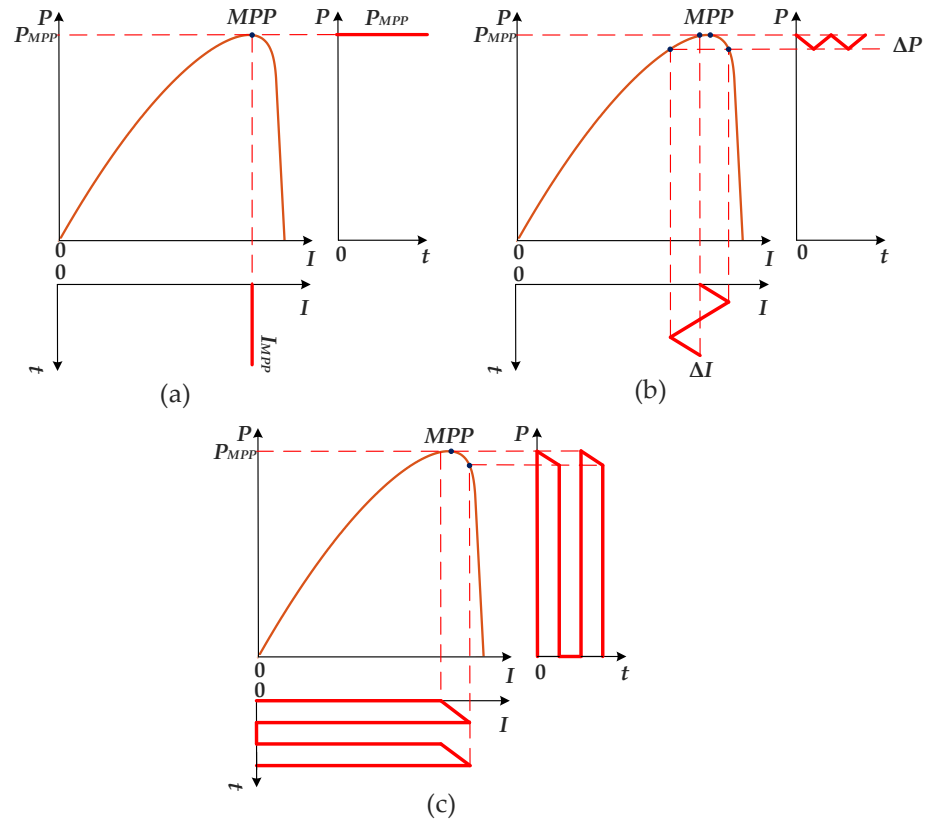


Figure 3. The Impact of MPPT input current shape on the value of solar battery power: (a) continuous current; (b) current with ripple ΔI ; (c) discontinuous current.

There is an input inductor L in the boost converter [12]. This inductor produces continuous current and can be used directly as an MPPT (Figure 4a). Because it has a series-connected transistor, buck and buck/boost converters have an extra capacitor C_F that filters the input current, as shown in Figure 4b.

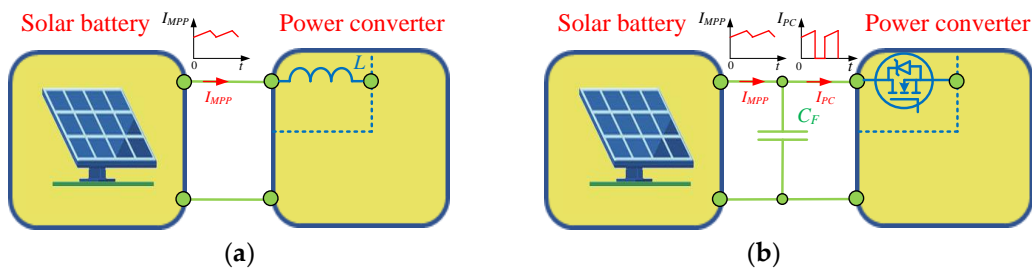


Figure 4. Providing continuous current: (a) natural for power converters with the series-connected inductor L ; (b) with an additional capacitor C_F for a converter with a series transistor.

The equivalent resistance of solar battery, R_{SB} , varies as a function of solar insolation power and is greater than the minimum value $R_{SB(\min)}$ attained for maximum insolation:

$$R_{SB(\min)} = \frac{U_{MPP}}{I_{MPP}} \Big|_{P_{SB} \rightarrow \max} \quad (3)$$

When solar insolation is zero, R_{SB} tends to infinity. In practice, MPPT works effectively with some range of solar battery resistance $R_{SB} \in [R_{SB(\min)}; R_{SB(\max)}]$, where $R_{SB(\max)}$ defines the minimum solar insolation power $P_{SB(\min)}$ where MPPT may operate [13,14]. Therefore, MPPT has to effectively shift the operating point of the solar battery to MPP in the defined range of resistance R_{SB} . MPPT converters with different voltage gains G are used depending on the relationship between the resistances of a solar battery R_{SB} and the load R_L :

- Boost converters ($G > 1$), if $R_{SB(\max)} < R_L$;
- Buck/boost converters ($G = G_{(\min)} \dots 1 \dots G_{(\max)}$), if $R_{SB(\min)} < R_L < R_{SB(\max)}$;
- Buck converters ($G < 1$), if $R_{SB(\min)} > R_L$.

The common foregoing conditions of effective PV system design are complemented by the technical aspects of connecting the solar batteries to the power grid or its standalone operation. In Table 1, the topologies of common PV applications and their modifications are listed.

Table 1. Common PV application descriptions and requirements.

PV Application	Modifications
1. Standalone PV applications [15,16]	- DC or AC;
2. On-grid PV applications [17,18]	- with DC-link or without it (only for AC systems)
3. Hybrid PV applications [19,20]	- low, middle, or high voltage;
	- with electric battery or without it;
	- DC or AC battery connected;
	- isolated or transformerless;
	- one, three, or multiphase.

For the efficient design of PV systems, the key task is the correct choice of power converter topology for providing effective energy transfer and conversion. Therefore, it is necessary to pay attention to the following features of power converter design for PV systems:

1. The multifunctional purpose of the power converters is:
 - MPPT in a standalone DC or AC system simultaneously provides maximum power and charges an electric accumulator, as shown in Figure 5a,b [21];
 - In AC on-grid applications that directly deliver energy to the AC power grid, MPPT maximizes energy, converts it from DC to AC form, and provides power factor correction and reactive power generation as needed, as shown in Figure 5c [22].
2. Advanced schematic and control algorithms:
 - For energy balancing and stable generation, often for AC grid-connected applications, electric batteries with bidirectional chargers are connected [23], as shown in Figure 5c. To make sure that electricity has the right dynamics and quality, you need to use advanced control algorithms with multi-loop and predictive control [24].
 - Co-ordination of parallel operations of several energy sources and determination of their priority in a hybrid system [25], as seen in Figure 5d.
3. Special issues in converter design:
 - For high voltage DC and AC on-grid systems, specialized converters adapted for PV applications are being developed [26];

- Hybrid systems provide parallel operation of several alternative power supplies connected to the power grid and load that in general may be considered a multiport power system [27]. As a result, a reduced-component multiport power system can be made instead of having a lot of separate power converters that do the same thing [28].

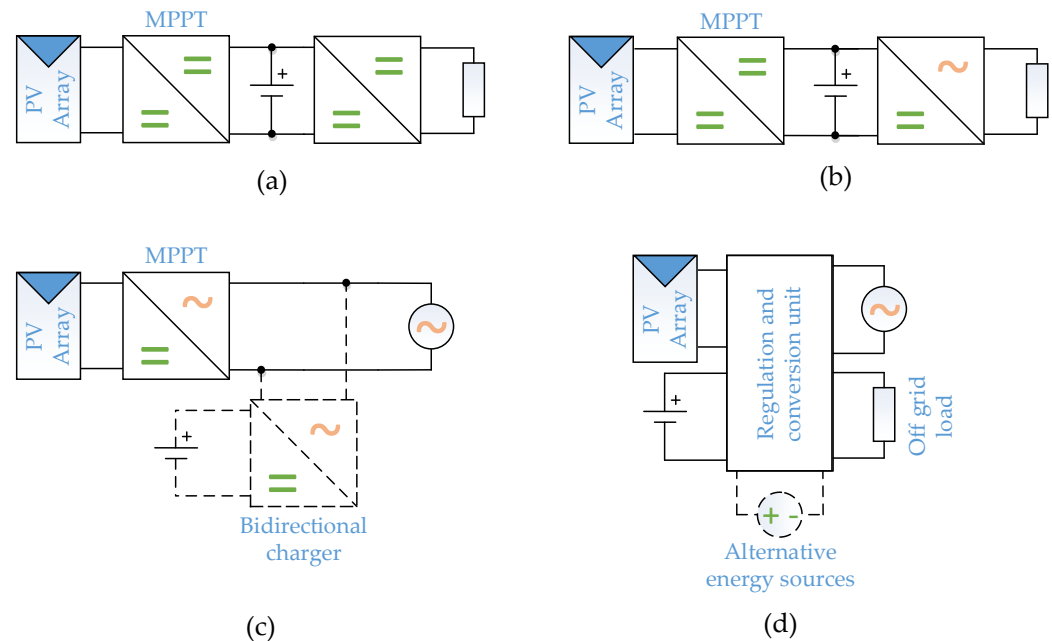


Figure 5. Common PV applications: (a) standalone DC systems; (b) standalone AC systems; (c) on-grid AC systems with energy storage; and (d) hybrid systems.

Implementation of the aforementioned PV applications is covered by a set of converter topologies with their own advantages and disadvantages. The choice of the most appropriate solution depends on many factors [29]:

- System type (standalone or grid-on, DC or AC);
- Voltage and power level (low, middle, or high);
- The relationship between the voltage of the solar battery and the grid;
- Additional requirements on power factor value and power stability.

For instance, an MPPT unit may be effectively realized with either a DC–AC converter or a two-stage power system with DC–DC and DC–AC converter; a storage system may be installed on the DC–DC side of the PV system or directly on the DC or AC system; a PV system may be connected to the grid with one or few high-power converters, or realized as a distributed system with a set of low or middle power converters, etc.

This paper looks at different topologies that could be used to solve the discussed problems. It also tries to show the good and bad points of the solutions based on proper generalization parameters that allow comparing their effectiveness.

In general, power converter comparative analysis is performed based on their complexity, i.e., number of inductors, capacitors, and semiconductor components [30], also taking into account voltage gain characteristics, control strategy, efficiency, etc. However, the most fruitful results are obtained by comparing converters designed to solve a particular problem that put forward a number of specific requirements to the power converter. For instance, for designing a dynamic voltage restorer [31], these parameters are high dynamics, wide reactive and active power regulation range, and easy energy storage integration, whereas for AC/DC Microgrids [32] parameters are the value of output impedance, type of power flow control, voltage modulation strategy, and voltage and frequency regulation. For solar applications, the main requirement, as mentioned before, is high efficiency in a wide power range and, as for industrial solutions, low cost per unit of power.

As a numerical criteria of the converter cost per unit of output power, P_{out} may be measured by the cost factor k_C which is inverse to the transistor utilization factor k_U [33]:

$$k_C = \frac{1}{k_U} = \frac{S}{P_{out}}, \quad (4)$$

where S is total switch stress and:

$$S = \sum_{k=1}^N U_{kmax} \cdot I_{kmax}, \quad (5)$$

where N is the switch number of the power converter, and U_{kmax} and I_{kmax} are the maximum voltage and current stress of the switch k , respectively. Normalized power loss P^* [34] of the switch can be used to estimate power converter efficiency.

Detailed and comprehensive comparative PV converter analysis in space of cost factor and normalized power loss is carried out in the paper in such a sequence.

Section 2 discloses a methodology of deriving cost factor and normalized power loss for DC–DC and DC–AC converters with hard and soft-switching transistor commutation.

In Sections 3–6, classification, cost, and efficiency comparisons of power converters for AC grid, energy storage, high voltage gain, and hybrid PV applications are given.

Discussion (Section 7) deals with the overall analysis of PV application design and recommendations.

2. Materials and Methods

According to standards for solar batteries and inverters [35–38], the maximum operating voltage of PV equipment currently does not exceed $U_{max} = 1500$ V. In this case, the converter is connected to 1–3 solar battery strings with a short-circuit current of 10 A per string. Application design with such operating voltage and current, as usual, is performed based on Si IGBT or SiC MOSFET transistors [39]. Due to less static and dynamic power loss, and a permanent price reduction in SiC transistors, Cree C2M0080170P is used for loss calculation [40]. Static loss of the transistor P_{st}^* with a constant current I_{DC} that provides output power P_{out} at voltage U_{max} is normalized and defined as $P_{Tst}^* = 1$ p.u. It is well known that the resistance $R_{DS(on)}$ of SiC and MOSFET transistors quadratically increases with voltage. Additionally, power loss depends on transistor current shape, which in a general case for DC–DC converters is shown in Figure 6. There are shown peak and minimum transistor values, I_{peak} and I_{min} , correspondingly. Average value of transistor I_{Tav} on interval DT is calculated as $I_{Tav} = (I_{peak} + I_{min})/2$.

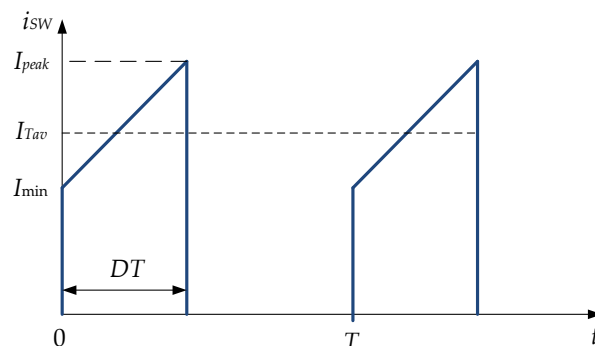


Figure 6. The current shape of a transistor in a DC–DC hard-switching converter.

Thus, the RMS value of $I_{SW(RMS)}$ compared with I_{DC} is calculated as follows:

$$\frac{I_{SW(RMS)}}{I_{DC}} = \frac{\sqrt{D(I_{peak}^2 + I_{peak}I_{min} + I_{min}^2)}}{\sqrt{3}I_{DC}} = k_{Tst}\sqrt{\frac{D}{3}}, \quad (6)$$

where k_{Tst} is the factor that depends on converter topology.

If there is no pulsation in the current, $I_{peak} = I_{min} = I_{Tav}$, and the RMS value is calculated using the average transistor current value I_{Tav} on the interval DT:

$$\frac{I_{SW(RMS)}}{I_{DC}} = \frac{I_{Tav}}{I_{DC}} \sqrt{D}.$$

Therefore, k switch power loss $P_{Tst(k)ht}^*$ for hard-switching converters with overvoltage U_{kmax} is defined as:

$$P_{Tst(k)ht}^* = P_{Tst}^* \left(\frac{U_{kmax}}{U_{max}} \right)^2 \frac{D(I_{peak}^2 + I_{peak}I_{min} + I_{min}^2)}{3I_{DC}^2} = \frac{D}{3} k_{Tst(k)}^2 \left(\frac{U_{kmax}}{U_{max}} \right)^2, \quad (7)$$

Whereas in resonant converters with sine wave current shape, the power loss $P_{Tst(k)s}^*$ is multiplied by shape factor $k_{sh} = \pi^2/8$ [41]:

$$P_{Tst(k)s}^* = \frac{\pi^2}{8} D k_{Tst(k)}^2 \left(\frac{U_{kmax}}{U_{max}} \right)^2. \quad (8)$$

Due to the nearly rectangular shape of the current in soft-switching converters, the static power loss is considered the same as for constant current P_{Tst}^* .

The dynamic power loss P_{Td}^* for hard-switching mode is calculated using a comparison of transistor static and dynamic losses at maximum power $I_{DC} = 30$ A, $U_{max} = 1500$ V at switching frequency $f_{sw} = 40$ kHz, $P_{Td}^* = 0.5$ p.u. The dynamic loss $P_{T(k)d}^*$ for defined transistor current I_{Tk} and voltage U_{Tk} is:

$$P_{Td(k)}^* = P_{Td}^* \left(\frac{U_{Tk}}{U_{max}} \right) \left(\frac{I_{Tk}}{I_{DC}} \right) = 0.5 \left(\frac{U_{Tk}}{U_{max}} \right) \left(\frac{I_{Tk}}{I_{DC}} \right). \quad (9)$$

It is considered that in resonant and soft-switching converters, dynamical loss is absent.

A diode's static power loss P_{Dst}^* is calculated based on Cree C5D25170H [42] and expressed in units of P_{Tst}^* , $P_{Dst}^* = 0.8$ p.u for constant current I_{DC} . If the diode's forward V_D is assumed to be constant and proportional to reverse voltage U_{kmax} , its static loss for the hard-switching converter is calculated as follows:

$$P_{Dst(k)hd}^* = P_{Dst}^* k_{Dst(k)} \left(\frac{U_{kmax}}{U_{max}} \right) (1 - D) = \frac{0.8 k_{Dst(k)} U_{kmax} (1 - D)}{U_{max}}, \quad (10)$$

where $k_{Dst(k)}$ is the relationship between the average value of the diode current I_{Dk} on the interval $(1 - D)$ to current I_{DC} :

$$k_{Dst(k)} = \frac{I_{Dk}}{I_{DC}}, \quad (11)$$

whereas in the case of soft-switching:

$$P_{Dst(k)s}^* = P_{Dst}^* k_{Dst(k)} \frac{\pi}{2\sqrt{2}} \left(\frac{U_{kmax}}{U_{max}} \right) (1 - D) = \frac{0.8 k_{Dst(k)} \pi U_{kmax} (1 - D)}{2\sqrt{2} U_{max}}. \quad (12)$$

Dynamic loss of the diode for current I_{DC} is $P_{Dd}^* = 1$ p.u. For defined diode current I_{Dk} and voltage U_{Dk} , dynamic loss $P_{D(k)d}^*$ is calculated similarly to the Formula (9):

$$P_{Dd(k)}^* = P_{Dd}^* \left(\frac{U_{Dk}}{U_{max}} \right) \left(\frac{I_{Dk}}{I_{DC}} \right) = \left(\frac{U_{Dk}}{U_{max}} \right) \left(\frac{I_{Dk}}{I_{DC}} \right). \quad (13)$$

The final values of static and dynamic power losses for DC-DC converters are given in Table 2.

Table 2. Normalized power loss of the transistor and diode for DC–DC converters.

Power Loss Type	Converter Type		
	Hard-Switching	Soft-Switching	Resonant
Transistor static power loss, P_{Tst}^*	$\frac{D}{3} k_{Tst(k)}^2 \left(\frac{U_{kmax}}{U_{max}}\right)^2$	$\frac{D}{3} k_{Tst(k)}^2 \left(\frac{U_{kmax}}{U_{max}}\right)^2$	$\frac{\pi^2 D}{8} k_{Tst(k)}^2 \left(\frac{U_{kmax}}{U_{max}}\right)^2$
Transistor dynamic power loss, P_{Td}^*	$\frac{0.5 U_{Tk} I_{Tk}}{U_{max} I_{DC}}$	0	0
Diode static power loss, P_{Dst}^*	$\frac{0.8 k_{Dst(k)} U_{kmax} (1-D)}{U_{max}}$	$\frac{0.8 k_{Dst(k)} U_{kmax} (1-D)}{U_{max}}$	$\frac{0.8 k_{Dst(k)} \pi U_{kmax} (1-D)}{2\sqrt{2} U_{max}}$
Diode dynamic power loss, P_{Dd}^*	$\frac{0.5 U_{Dk} I_{Dk}}{U_{max} I_{DC}}$	0	0

For DC–AC and AC–DC converter output, AC side voltage and current are sinusoidal; therefore, diodes and transistor current, as well as power loss, depend on grid voltage phase $\varphi = 2\pi \cdot t / T_f$, where T_f is the fundamental period of the grid voltage that is shown in Figure 7.

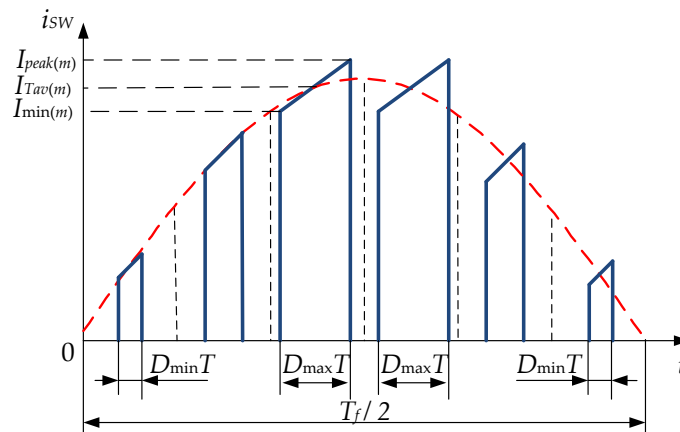


Figure 7. Transistor current shape for AC–DC and DC–AC hard-switching converters.

The amplitude peak current values $I_{peak(m)}$, $I_{Tav(m)}$, and $I_{min(m)}$ are used to calculate the AC shaped current cost factor k_c , whereas the power loss $P_{con(AC)}^*$ analysis is performed based on the integration of instantaneous power loss $P_{con(AC)}^*$ from Table 2, where duty cycle D is a function of power grid phase φ , $D [0; D_{max}]$, and normalized with current i_{norm} :

$$P_{con(AC)}^* = \frac{1}{2\pi} \int_0^{2\pi} P_{con}^*(\varphi) i_{norm} d\varphi, \tag{14}$$

where $i_{norm} = \pi \cdot \sin(\varphi) / 2$ has a half-period average value of unity:

$$\frac{1}{\pi} \int_0^{\pi} i_{norm} d\varphi = 1. \tag{15}$$

Thus, equations have been derived that can be used to calculate the total converter power loss P_{con}^* and the cost factor k_c for both AC and DC applications. These numbers are used to compare different PV applications with different converters for each type of PV.

3. AC Grid on PV Applications

AC grid-connected renewable applications aim to deliver the maximum possible energy to the grid as efficiently as possible. This will be accomplished using single-stage

or two-stage systems. The single-stage application is an inverter that simultaneously performs the functions of MPPT, boosting, and voltage conversion from DC to AC [43]. In the two-stage converter, these functions are split between DC–DC and DC–AC inverters [44]. Depending on the safety conditions or voltage gain requirements, applications may be equipped with transformers or be transformerless. Typical structures of on-grid applications are shown in Figure 8.

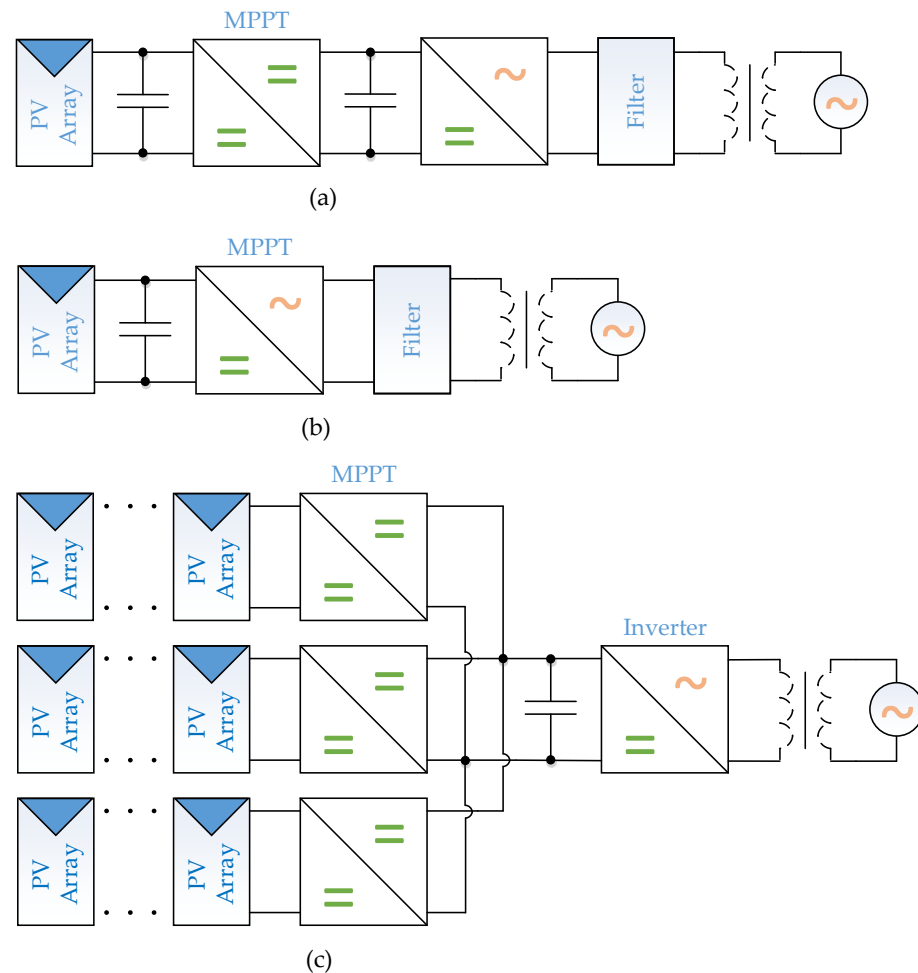


Figure 8. On-grid application structures that are commonly used include: (a) two-stage on-grid application; (b) single-stage on-grid application; and (c) distributed two-stage applications.

In terms of improving efficiency and reducing the cost of the system, single-stage systems have clear advantages over two-stage. Nevertheless, two-stage systems are actively used due to simple system control and the opportunity to connect energy storage to DC-link or design multi-string PV systems [45]. In two-stage systems, any non-isolated DC–DC converter can be used as MPPT [12], but mostly boost, buck, and buck-boost converters are used due to less transistor stress [46]. For reducing power loss, soft-switching [47] or interleaved converters [48,49] are used.

As usual, single-phase or three-phase bridge topologies are implemented for the design of DC–AC converters in single and two-stage topologies [50]. Soft-switching commutation and reduced power loss are possible with advanced control methods [51,52].

Non-isolated one-phase inverters with common full or half-bridge topology suffer from leakage current that flows between AC grid ground and PV through parasitic capacitors [53] and brings about safety and interference issues [54]. Additional transistors implemented in H5, H6, HERIC, and hybrid-bridge topologies [55] cut off the leakage current path and eliminate it. For transistor overvoltage limitation, multilevel inverters,

for instance, 3L-NPC [56] and 3L-SC [57], are used. The aforementioned DC–AC PV application schematics are illustrated in Figure 9 and listed in Table 3 for one stage DC–DC and DC–AC converters, respectively, with cost factor k_C and normalized power loss of the converter P_{con}^* .

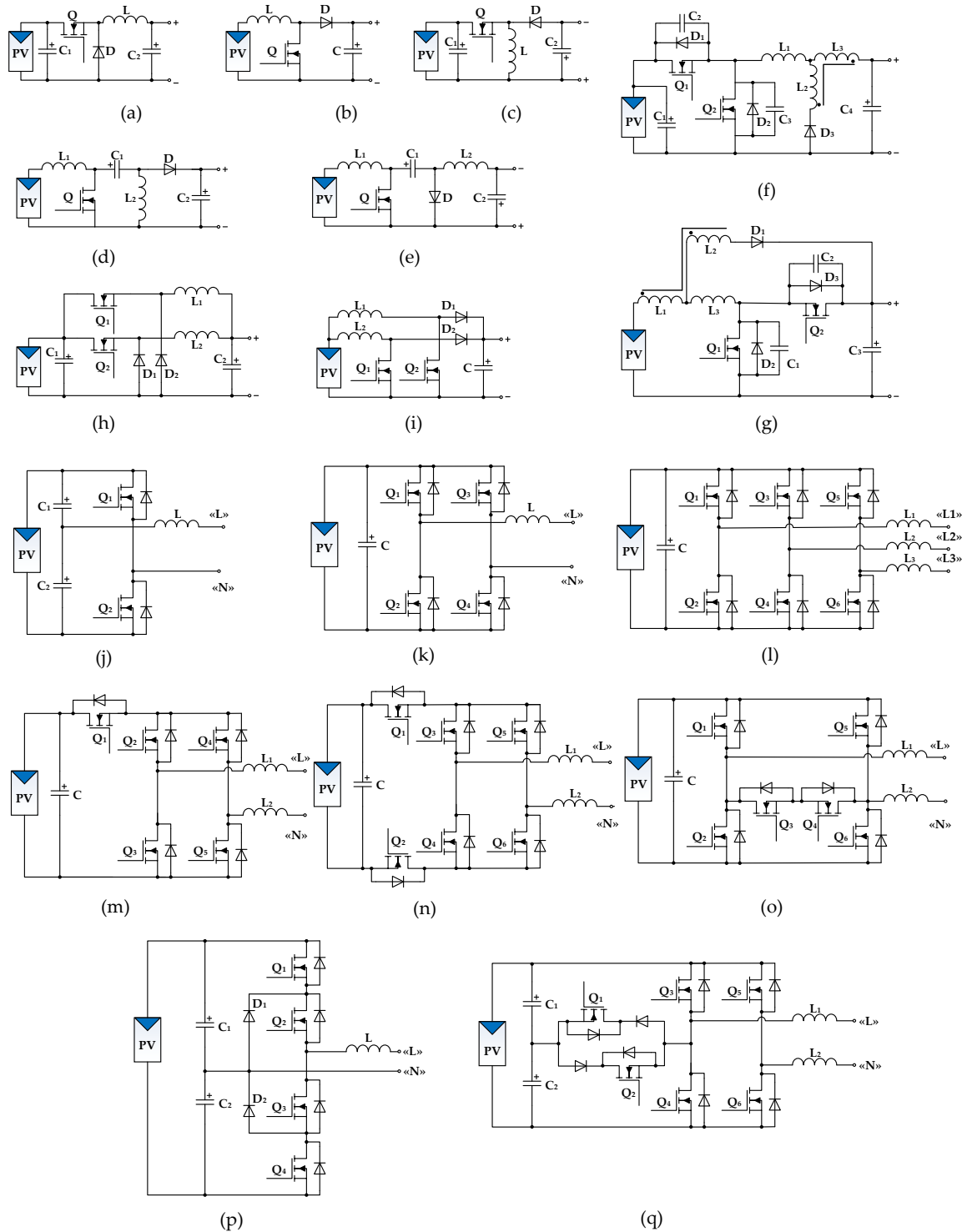


Figure 9. Converter topologies for grid-based applications: (a) buck; (b) boost; (c) buck-boost; (d) SEPIC; (e) Cuk'; (f) soft-switching buck; (g) soft-switching boost; (h) interleaved buck; (i) interleaved boost; (j) half-bridge; (k) full-bridge; (l) three phase full-bridge; (m) H5; (n) H6; (o) HERIC; (p) 3L-NPC; (q) 3L-SC.

Table 3. The cost factor k_C and the normalized power loss for common DC–DC and DC–AC converters.

Converter Topology	k_C	P_{con}^*
DC–DC converters		
Buck [12], Figure 9a	$\frac{I_{peak}}{D I_{Tav}}$	$\frac{4}{3D} \left(1 - \frac{I_{peak} I_{min}}{(I_{peak} + I_{min})^2} \right) + \frac{0.8(1-D)}{D} + \frac{I_{peak}}{D I_{Tav}}$
Boost [12], Figure 9b	$\frac{I_{peak}}{D(1-D) I_{Tav}}$	$\frac{4D}{3(1-D)^2} \left(1 - \frac{I_{peak} I_{min}}{(I_{peak} + I_{min})^2} \right) + 0.8 + \frac{I_{peak}}{(1-D) I_{Tav}}$
Buck-boost, SEPIC, Cuk' [12], Figure 9c–e	$\frac{I_{peak}}{D(1-D) I_{Tav}}$	$\frac{4}{3D(1-D)^2} \left(1 - \frac{I_{peak} I_{min}}{(I_{peak} + I_{min})^2} \right) + \frac{0.8}{D} + \frac{I_{peak}}{(1-D) D I_{Tav}}$
Soft-switching buck [47], Figure 9f	$\frac{2I_{peak}}{D I_{Tav}}$	$\frac{4}{3D} \left(1 - \frac{I_{peak} I_{min}}{(I_{peak} + I_{min})^2} \right) + \frac{0.8(1-D)}{D}$
Soft-switching boost [47], Figure 9g	$\frac{2I_{peak}}{(1-D) I_{Tav}}$	$\frac{4D}{3(1-D)^2} \left(1 - \frac{I_{peak} I_{min}}{(I_{peak} + I_{min})^2} \right) + 0.8$
Interleaved buck [48], Figure 9h, m cells	$\frac{I_{peak}}{D I_{Tav}}$	$\frac{4}{3Dm} \left(1 - \frac{I_{peak} I_{min}}{(I_{peak} + I_{min})^2} \right) + \frac{0.8(1-D)}{D} + \frac{I_{peak}}{Dm I_{Tav}}$
Interleaved boost [49], Figure 9i, m cells	$\frac{I_{peak}}{(1-D) I_{Tav}}$	$\frac{4D}{3(1-D)^2 m} \left(1 - \frac{I_{peak} I_{min}}{(I_{peak} + I_{min})^2} \right) + 0.8 + \frac{I_{peak}}{(1-D) m I_{Tav}}$
DC–AC converters		
Half-bridge [50], Figure 9j	$\frac{8I_{peak(m)}}{D_{max} I_{Tav(m)}}$	$\frac{4\pi^2}{3D_{max}^2} \left(1 - \frac{I_{peak(m)} I_{min(m)}}{(I_{peak(m)} + I_{min(m)})^2} \right) + \frac{1.6}{D_{max}} \left(\frac{\pi}{2} + 1 \right) + \frac{2I_{peak(m)}}{D_{max} I_{Tav(m)}}$
Full-bridge [50], Figure 9k	$\frac{8I_{peak(m)}}{D_{max} I_{Tav(m)}}$	$\left(\frac{2\pi}{3D_{max}} + \frac{\pi^2}{3D_{max}^2} \right) \left(1 - \frac{I_{peak(m)} I_{min(m)}}{(I_{peak(m)} + I_{min(m)})^2} \right) + \frac{0.8}{D_{max}} \left(\frac{\pi}{2} + 1 \right) + \frac{I_{peak(m)}}{D_{max} I_{Tav(m)}}$
Triple-bridge [50], Figure 9l	$\frac{12I_{peak(m)}}{\sqrt{3} D_{max} I_{Tav(m)}}$	$\frac{2\pi}{9D_{max}} \left(1 - \frac{I_{peak(m)} I_{min(m)}}{(I_{peak(m)} + I_{min(m)})^2} \right) + \frac{0.8}{D_{max}} \left(\frac{\pi}{2} + 1 \right) + \frac{I_{peak(m)}}{D_{max} I_{Tav(m)}}$
H5 [55], Figure 9m	$\frac{10I_{peak(m)}}{D_{max} I_{Tav(m)}}$	$\left(\frac{2\pi}{3D_{max}} + \frac{\pi^2}{3D_{max}^2} \right) \left(1 - \frac{I_{peak(m)} I_{min(m)}}{(I_{peak(m)} + I_{min(m)})^2} \right) + \frac{0.8}{D_{max}} \left(\frac{\pi}{2} + 1 \right) + \frac{1.5I_{peak(m)}}{D_{max} I_{Tav(m)}}$
H6 [55], Figure 9n	$\frac{12I_{peak(m)}}{D_{max} I_{Tav(m)}}$	$\left(\frac{2\pi}{D_{max}} + \frac{\pi^2}{3D_{max}^2} \right) \left(1 - \frac{I_{peak(m)} I_{min(m)}}{(I_{peak(m)} + I_{min(m)})^2} \right) + \frac{0.8}{D_{max}} \left(\frac{\pi}{2} + 1 \right) + \frac{1.5I_{peak(m)}}{D_{max} I_{Tav(m)}}$
HERIC [55], Figure 9o	$\frac{12I_{peak(m)}}{D_{max} I_{Tav(m)}}$	$\left(\frac{2\pi}{3D_{max}} + \frac{\pi^2}{3D_{max}^2} \right) \left(1 - \frac{I_{peak(m)} I_{min(m)}}{(I_{peak(m)} + I_{min(m)})^2} \right) + \frac{0.8}{D_{max}} \left(\frac{\pi}{2} + 1 \right) + \frac{1.5I_{peak(m)}}{D_{max} I_{Tav(m)}}$
3L-NPC [56], Figure 9p	$\frac{8I_{peak(m)}}{D_1 I_{Tav(m)}}$	$\left(\frac{2\pi}{3D_{max}} + \frac{\pi^2}{3D_{max}^2} \right) \left(1 - \frac{I_{peak(m)} I_{min(m)}}{(I_{peak(m)} + I_{min(m)})^2} \right) + \frac{0.8}{D_{max}} \left(\frac{\pi}{2} + 1 \right) + \frac{I_{peak(m)}}{D_{max} I_{Tav(m)}}$
3L-SC [57], Figure 9q	$\frac{10I_{peak(m)}}{D_1 I_{Tav(m)}}$	$\left(\frac{\pi}{2D_{max}} + \frac{5\pi^2}{12D_{max}^2} \right) \left(1 - \frac{I_{peak(m)} I_{min(m)}}{(I_{peak(m)} + I_{min(m)})^2} \right) + \frac{0.8}{D_{max}} \left(\frac{\pi}{2} + 1 \right) + \frac{I_{peak(m)}}{D_{max} I_{Tav(m)}}$

Because low current ripple ΔI is a key requirement of the grid on applications for sufficient power factor, the majority of converters use $I_{min} = 0.9 I_{Tav(m)}$, $I_{peak} = 1.1 I_{Tav}$. However, interleaved converters operate in boundary mode, when $I_{min} = 0$ and $I_{peak} = 2 I_{Tav}$. Based on the aforementioned assumptions, the cost factor k_C and normalized power loss P_{con}^* of DC–DC converters are shown in Figure 10a,b, respectively. The same curves for DC–AC converters are shown in Figure 11a,b.

Because of a larger number of transistors, DC–AC converters are weaker in terms of parameter values k_C and P_{con}^* than their DC–DC counterparts. Among DC–DC converters, the most effective solutions are based on buck and boost converters. Whereas buck-boost solutions (buck-boost, SEPIC, Cuk' converters) increase costs and losses. interleaved converters allow for reduced losses at the expense of an increase in price and dimensions.

Among DC–AC converters, three-phase is the most efficient converter because of the minimum number of transistors per phase. For single-phase applications, full-bridge, H5, H6, and HERIC converters have very similar k_C and P_{con}^* values.

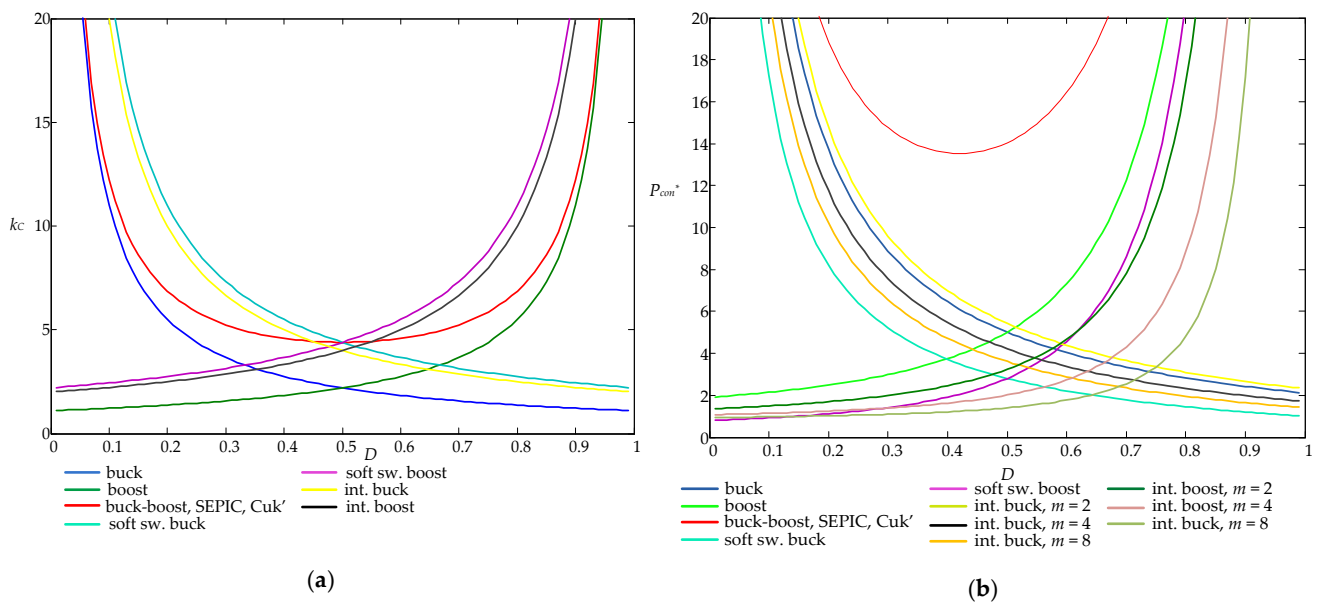


Figure 10. DC-DC converters: (a) cost factor k_C ; (b) normalized power loss P_{con}^* .

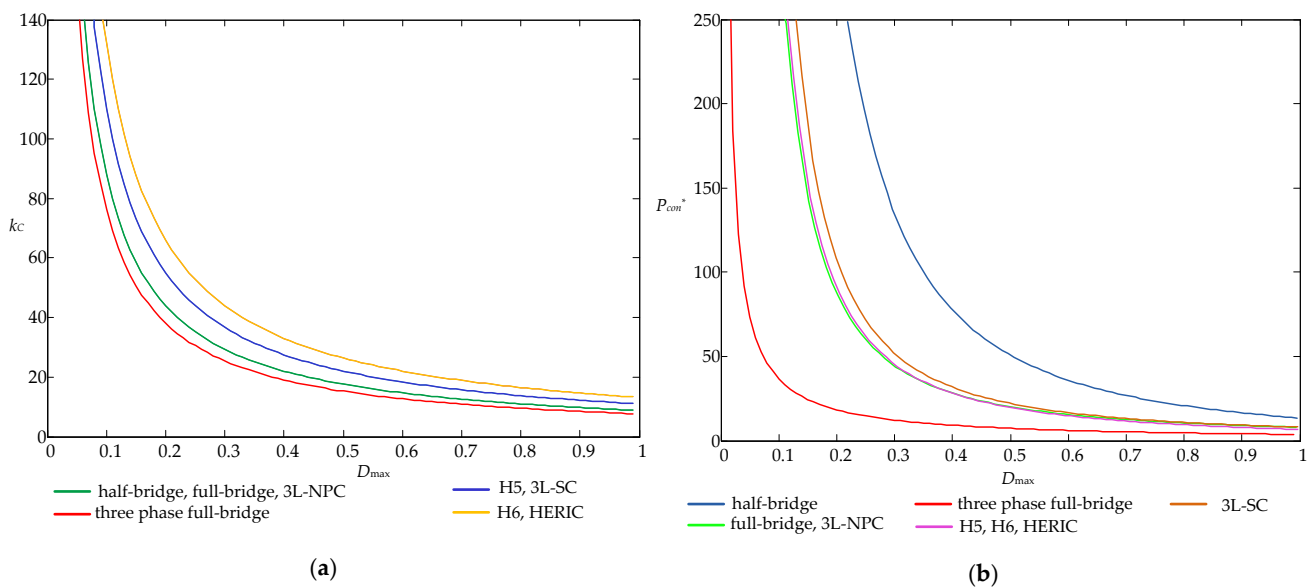


Figure 11. DC-AC converters: (a) cost factor k_C ; (b) normalized power loss P_{con}^* .

Two-stage DC-AC applications may be used for PV applications in the following cases:

- Boosting DC voltage;
- Decreasing k_C and P_{con}^* to allow for a wider range of input/output voltage operations;
- Inconsistency of power grid and solar battery voltages.

In a two-stage system, voltage regulation is performed at the DC-DC stage, whereas the DC-AC stage operates with the maximum duty cycle, $D_{max} \rightarrow 1$, that provides minimum power loss. For instance, Figure 12a compares the cost factor k_C of single-stage applications based on a full-bridge converter and a two-stage application designed on buck and full-bridge converters. Figure 12b compares power loss for the same configurations with $D_{max} = 1$ for the DC-AC converter of the two-stage system. Formulas for the considered cases are shown in Table 4.

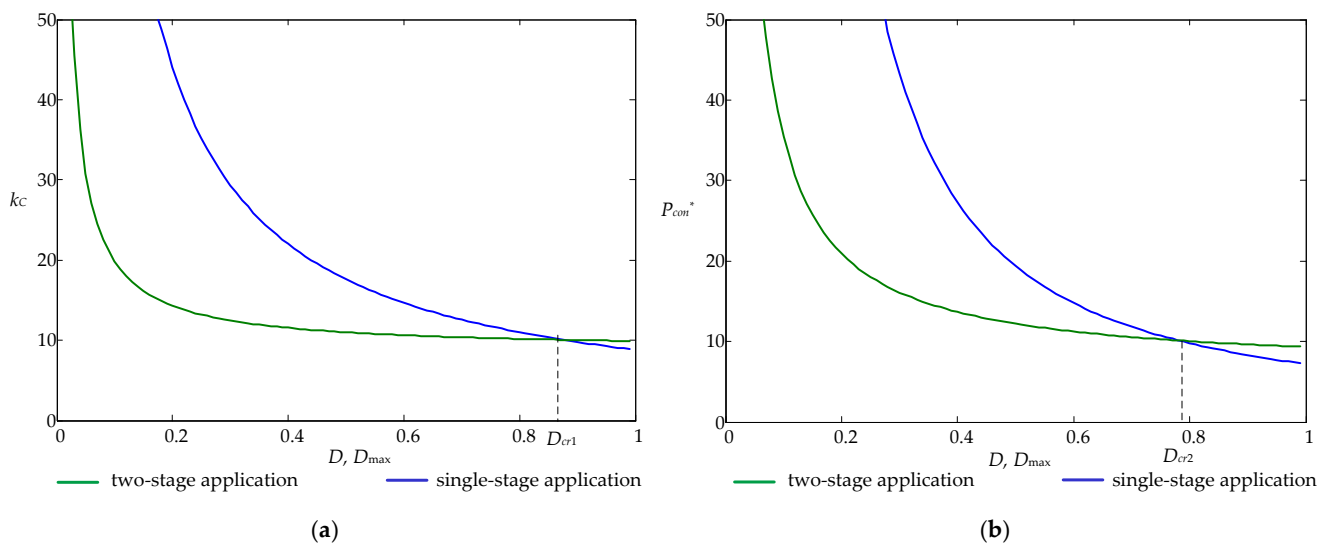


Figure 12. DC-AC converters: (a) the cost factor k_C ; (b) the normalized power loss P_{con}^* .

Table 4. The full-bridge converter is used to calculate the cost factor k_C and the normalized power loss for single- and two-stage applications.

	k_C	P_{con}^*
Single-stage application with a full-bridge converter	$\frac{8I_{peak(m)}}{D_{max}I_{Tav(m)}}$	$\left(\frac{2\pi}{3D_{max}} + \frac{\pi^2}{3D_{max}^2}\right) \left(1 - \frac{I_{peak(m)}I_{min(m)}}{(I_{peak(m)}+I_{min(m)})^2}\right) + \frac{0.8}{D_{max}} \left(\frac{\pi}{2} + 1\right) + \frac{I_{peak(m)}}{D_{max}I_{Tav(m)}}$
Two-stage application with buck and full-bridge converters	$\frac{I_{peak(m)}}{I_{Tav(m)}} \left(8 + \frac{1}{D}\right)$	$\left(\frac{2\pi}{3} + \frac{\pi^2}{3} + \frac{4}{3D}\right) \left(1 - \frac{I_{peak(m)}I_{min(m)}}{(I_{peak(m)}+I_{min(m)})^2}\right) + 0.8\left(\frac{\pi}{2} + 1\right) + \frac{I_{peak(m)}}{I_{Tav(m)}} \left(1 + \frac{1}{D}\right) + \frac{0.8(1-D)}{D}$

Figure 12 shows that for $D_{max} < D_{cr1} = 0.87$ and $D_{max} < D_{cr2} = 0.78$, the two-stage system has a lower cost factor k_C and a lower power loss P_{con}^* than the one-stage system. This means that the two-stage system is more efficient than the one-stage system.

Aside from energy-delivery, common DC-AC applications have additional functionality [58]:

- Voltage conversion and power grid synchronization;
- Disconnection and anti-islanding protection when power grid fault appears; Correction of the power factor of the input current.

The rapid evolution of on-grid PV applications with unstable generation complicates the grid’s stable operation. Due to the common DC-AC application’s disconnection from the power grid fault, the grid operation only worsened and became unbalanced. As a result, using converters with advanced functions that remain connected to the grid during faults and attempt to maintain a stable operation not only mitigates the impact of renewable energy instability, but also creates additional opportunities for power grid control and improves reliability [59].

The list of additional converter functions that improve power grid operation and converter control approaches, as well as topologies that may perform them, are given in Table 5.

Table 5. List of additional converter functions.

Opportunities for Power Grid Control	Converter Function	Control Strategy
Reactive power control [58]	Independent reactive and active power generation	Sinusoidal pulse width modulation (SPWM), space vector modulation (SVM) or hysteresis modulation in dq or $\alpha\beta$ space For frequency synchronization: zero-crossing method and the
Voltage stabilization [60–65]	Voltage and frequency ride through, voltage sag detection, reactive power generation	phase-locked-loop. For sag detection: RMS value estimator, synchronous rotating reference frame, wavelet, and Fourier transform. For power generation: SPWM, SVM or hysteresis modulation in dq or $\alpha\beta$ space
Grid power quality control [62]	Controlled injected current	SPWM or hysteresis modulation, frequency synchronization

As usual, the inverter's advanced functions are realized with basic inverter topologies with improved control strategies and require no extra elements except for sensors.

4. Energy Storage Applications

An energy storage system is an integral part of renewable power supply systems. The main purpose of the storage system is to provide a powerful balancing of unstable renewable sources that operate at MPP and variable load. Typical converter topologies of energy storage applications are shown in Figure 13.

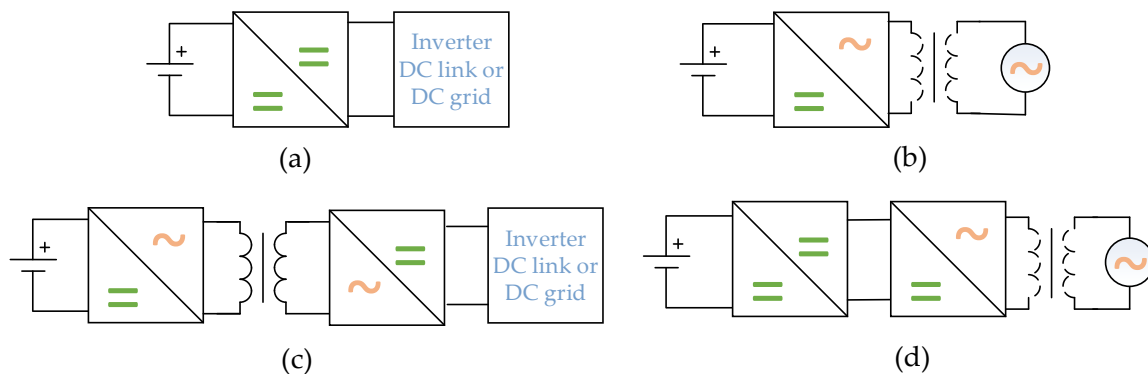


Figure 13. The following are typical energy storage converter topologies: (a) single-stage DC–DC application; (b) single-stage DC–AC application; (c) two-stage isolated DC–DC application; (d) two-stage DC–AC application.

Single-stage DC–DC and DC–AC topologies in Figure 13a and 13b respectively have simple structures and functionality. DC–DC converters for built-in energy storage connect to two-stage on-grid PV inverters or DC power grids, whereas DC–AC topologies are connected directly to the AC power grid. Figure 13c,d are used for energy storage isolation in DC power grids or AC grids and provide much more functionality, i.e., multi-mode charging, a wide range of battery charging voltages and currents, advanced control, improved performance, and energy quality control.

With increasing renewable energy penetration, energy storage systems are becoming a necessary element to maintain stable grid operation. In particular, in the concepts of intelligent transmission and control of distributed systems FACTS [66], Smart Grid [67], and Vehicle to Grid (V2G) [68], energy storage is considered as a system-forming unit or unit that strongly improves the system operation, specifically:

- Load shifting occurs when renewable energy mostly charges the energy storage during the day, and the energy storage is discharged in the late hours of peak power demand [69];

- Shutdown protection in smart distributed power grids that allows supplying end-users when loss of power arises [70];
- Energy quality control (voltage, frequency, reactive power compensation, high harmonic reduction) [71].

Therefore, distributed systems usually use a single common storage system which improves the functioning of the entire system.

Because of the unstable generation of renewable sources, energy storage is permanently switched between charge and discharge modes with the unstable current. Therefore, energy storage control is much more intelligent than for a common charging device [72,73].

For DC–DC in stage energy storage applications, some of the converters discussed in the section about grid applications with modified control laws, such as full or half-bridge [74] and 3L-NPC [75] converters, require minor modifications and an increase in the number of transistors, for instance, SEPIC, Cuk' [76], or cascaded [77] and interleaved [78] half-bridge converters.

Electric isolation in DC applications is provided with a high-frequency transformer intermediate AC link. An AC link may be organized with dual full- or half-bridge converters and their soft-switching modifications [79–81].

Multi-level [82,83] or high-frequency link AC–AC converters [84] are used for single-stage AC applications, whereas full- and half-bridge converter modifications [85,86] are used for two-stage solutions.

Figure 14 depicts converters for single-stage storage applications, and Table 6 compares them based on the parameters k_C and P_{con}^* , whereas two-stage solutions are shown in Figure 15 and Table 7, respectively.

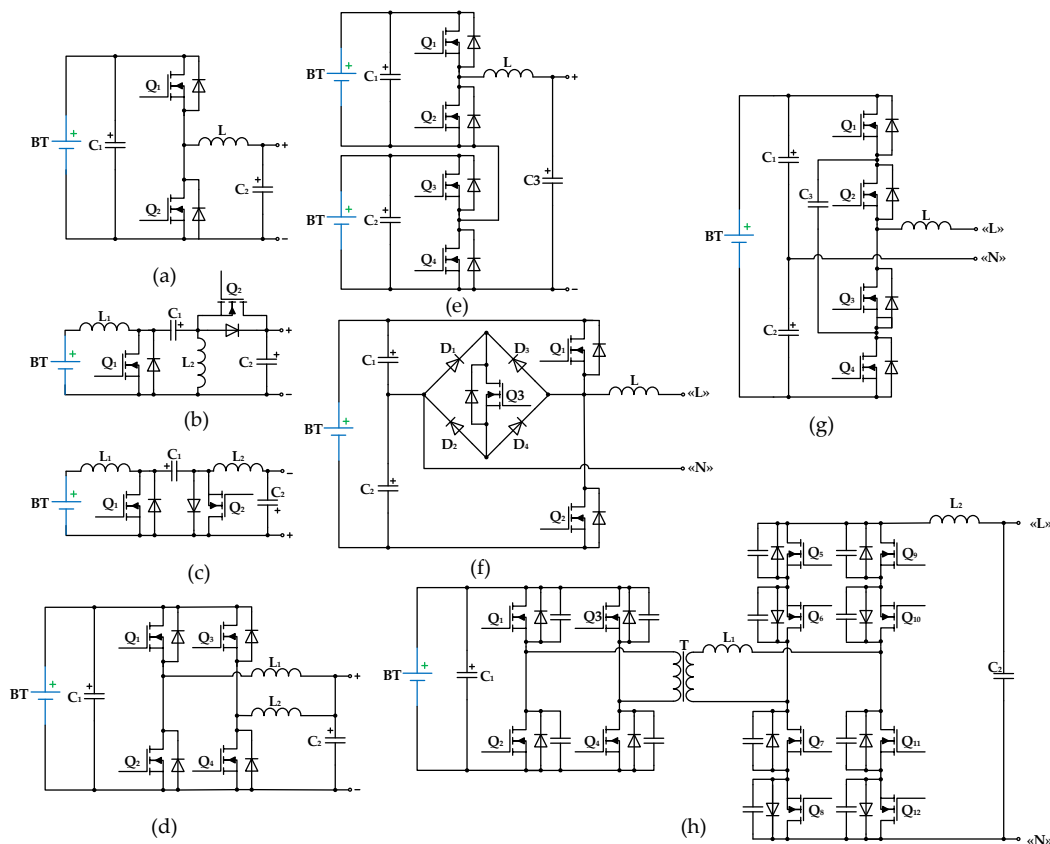


Figure 14. Converters for single-stage storage applications: (a) half-bridge; (b) Cuk'; (c) SEPIC/Luo; (d) interleaved half-bridge; (e) cascaded half-bridge; (f) half-bridge rectifier with neutral point switch clamped scheme; (g) capacitor clamped three-level; (h) high-frequency-link inverter.

Table 6. A Comparative analysis of single-stage energy storage converter effectiveness.

Converter Topology	k_C	P_{con}^*
DC–DC converters		
Half-bridge [74], Figure 14a	$\frac{4I_{peak}}{D_1 I_{Tav}}$	$\frac{4}{3D_1^2} \left(1 - \frac{I_{peak} I_{min}}{(I_{peak} + I_{min})^2} \right) + \frac{0.8}{D_1} + \frac{I_{peak}}{D_1 I_{Tav}}$
3L-NPC [75], Figure 9q	$\frac{4I_{peak}}{D_1 I_{Tav}}$	$\left(\frac{4}{3D_1} + \frac{4}{3D_1^2} \right) \left(1 - \frac{I_{peak} I_{min}}{(I_{peak} + I_{min})^2} \right) + \frac{0.8(1-D_1)}{D_1} + \frac{I_{peak}}{D_1 I_{Tav}}$
Cuk' [76], Figure 14b, SEPIC/Luo [76], Figure 14c	$\frac{2I_{peak}}{D_1(1-D_1) I_{Tav}}$	$\frac{4}{3D_1(1-D_1)^2} \left(1 - \frac{I_{peak} I_{min}}{(I_{peak} + I_{min})^2} \right) + \frac{0.4}{D_1(1-D_1)} + \frac{I_{peak}}{D_1(1-D_1) I_{Tav}}$
Interleaved half-bridge [77], Figure 14d	$\frac{2I_{peak}}{D_1 I_{Tav}}$	$\frac{2}{3mD_1^2} \left(1 - \frac{I_{peak} I_{min}}{(I_{peak} + I_{min})^2} \right) + \frac{0.8}{D_1} + \frac{I_{peak}}{D_1 I_{Tav}}$
If $U_{BT} > U_g \rightarrow$ Cascaded half-bridge [78], Figure 14e If $U_{BT} < U_g \rightarrow$	$\frac{2I_{peak}(1+D_1)}{D_1 I_{Tav}} \frac{2I_{peak}(2-D_1)}{(1-D_1) I_{Tav}}$	$\frac{4}{3D_1^2} \left(1 - \frac{I_{peak} I_{min}}{(I_{peak} + I_{min})^2} \right) + \frac{0.8}{D_1} + \frac{I_{peak}}{D_1(1-D_1) I_{Tav}} \frac{4}{3(1-D_1)^2} \left(1 - \frac{I_{peak} I_{min}}{(I_{peak} + I_{min})^2} \right) + \frac{0.8}{1-D_1} + \frac{I_{peak}}{D_1(1-D_1) I_{Tav}}$
DC–AC converters		
Half-bridge, Figure 9j	$\frac{8I_{peak(m)}}{D_{max1} I_{Tav(m)}}$	$\frac{4\pi^2}{3D_{max1}^2} \left(1 - \frac{I_{peak(m)} I_{min(m)}}{(I_{peak(m)} + I_{min(m)})^2} \right) + \frac{1.6}{D_{max1}} \left(\frac{\pi}{2} + 1 \right) + \frac{2I_{peak(m)}}{D_{max1} I_{Tav(m)}}$
Full-bridge, Figure 9k	$\frac{8I_{peak(m)}}{D_{max1} I_{Tav(m)}}$	$\left(\frac{2\pi}{3D_{max1}} + \frac{\pi^2}{3D_{max1}^2} \right) \left(1 - \frac{I_{peak(m)} I_{min(m)}}{(I_{peak(m)} + I_{min(m)})^2} \right) + \frac{0.8}{D_{max1}} \left(\frac{\pi}{2} + 1 \right) + \frac{I_{peak(m)}}{D_{max1} I_{Tav(m)}}$
Half-bridge rectifier with neutral point switch clamped scheme [82], Figure 14f	$\frac{5I_{peak(m)}}{D_{max1} I_{Tav(m)}}$	$\frac{4\pi^2}{3D_{max1}^2} \left(1 - \frac{I_{peak(m)} I_{min(m)}}{(I_{peak(m)} + I_{min(m)})^2} \right) + \frac{3.2}{D_{max1}} \left(\frac{\pi}{2} + 1 \right) + \frac{2I_{peak(m)}}{D_{max1} I_{Tav(m)}}$
Capacitor clamped three-level PWM converter [83], Figure 14g	$\frac{8I_{peak(m)}}{D_{max1} I_{Tav(m)}}$	$\frac{8\pi^2}{3D_{max1}^2} \left(1 - \frac{I_{peak(m)} I_{min(m)}}{(I_{peak(m)} + I_{min(m)})^2} \right) + \frac{0.5I_{peak(m)}}{D_{max1} I_{Tav(m)}}$
High-frequency link inverter [84], Figure 14h	$\frac{24I_{peak(m)}}{D_{max1} I_{Tav(m)}}$	$\left(\frac{2\pi}{D_{max}} + \frac{\pi^2}{3D_{max}^2} \right) \left(1 - \frac{I_{peak(m)} I_{min(m)}}{(I_{peak(m)} + I_{min(m)})^2} \right) + \frac{0.8}{D_{max}} \left(\frac{\pi}{2} + 1 \right) + \frac{3.2}{\pi}$

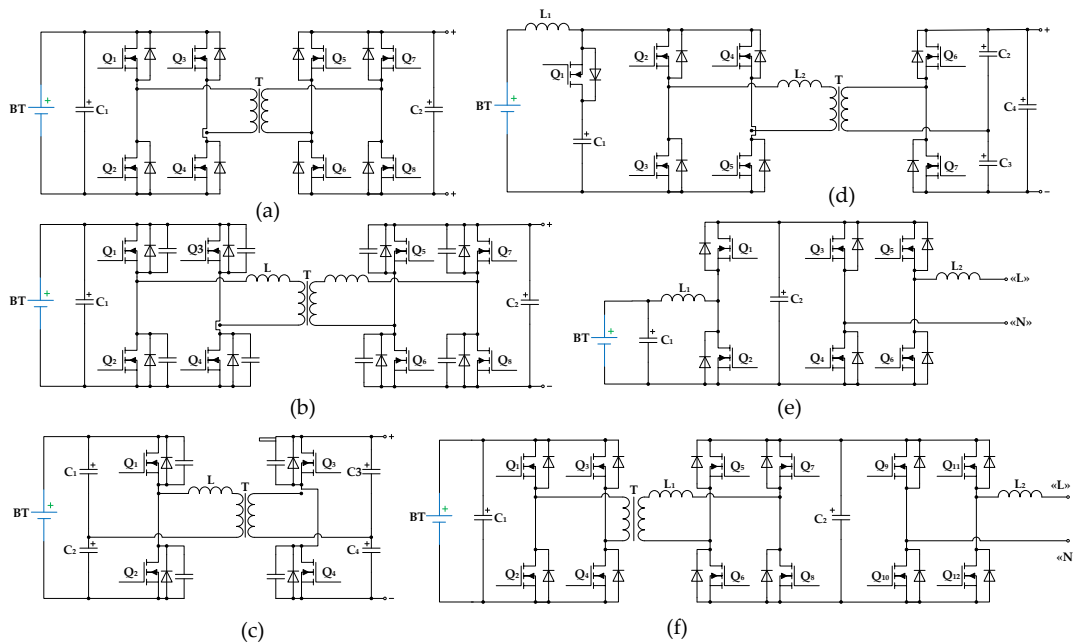


Figure 15. Converters for two-stage storage applications: (a) dual active bridge; (b) dual active bridge soft-switching; (c) with two voltage-fed half-bridges; (d) combined voltage-fed half-bridge and current-fed full-bridge; (e) half-bridge and full-bridge; (f) full-bridge DC–AC and dual active bridge DC–DC.

Table 7. A Comparative analysis of the two-stage energy storage converters' effectiveness.

Converter Topology	k_C	P_{con}^*
DC–DC converters		
Dual active bridge, Figure 15a	$\frac{8I_{peak}}{D_1 I_{Tav}}$	$\frac{4}{3D_1^2}(1 + D_1) \left(1 - \frac{I_{peak} I_{min}}{(I_{peak} + I_{min})^2}\right) + \frac{0.8}{D_1} + 0.8 + \frac{3I_{peak}}{D_1 I_{Tav}}$
Dual active bridge soft-switching [79], Figure 15b	$\frac{8I_{peak}}{D_1 I_{Tav}}$	$\frac{4}{3D_1^2}(1 + D_1) \left(1 - \frac{I_{peak} I_{min}}{(I_{peak} + I_{min})^2}\right) + \frac{0.8}{D_1} + 0.8$
Converter with two voltage-fed half-bridges [80], Figure 15c	$\frac{8I_{peak}}{D_1 I_{Tav}}$	8
Combined-voltage half-bridge and current-fed full-bridge [81], Figure 15d	$\frac{11I_{peak}}{(1-D_1)I_{Tav}}$	$\left(\frac{5+4D_1}{3(1-D_1)^2} + \frac{8(1-D_1)}{3D_1^2}\right) \left(1 - \frac{I_{peak} I_{min}}{(I_{peak} + I_{min})^2}\right) + \frac{0.8}{1-D_1}$
DC–AC converters		
Half-bridge and full-bridge [85], Figure 15e	$\frac{I_{peak(m)}}{I_{Tav(m)}} \left(\frac{8}{D_{max1}} + \frac{2}{(1-D_3)} \right)$	$\left(\frac{2\pi}{3D_{max1}} + \frac{\pi^2}{3D_{max1}^2} + \frac{4D_3}{3(1-D_3)^2} \right) \left(1 - \frac{I_{peak(m)} I_{min(m)}}{(I_{peak} + I_{min})^2} \right) + \frac{0.8}{D_{max1}} \left(\frac{\pi}{2} + 1 \right) + 0.8 + \frac{I_{peak(m)}}{I_{Tav(m)}} \left(\frac{1}{D_{max1}} + \frac{1}{(1-D_3)} \right)$
Full-bridge DC–AC and dual active bridge DC–DC [86], Figure 15f	$\frac{8I_{peak(m)}}{I_{Tav(m)}} \times \left(\frac{1}{D_{max1}} + \frac{1}{D_3} \right)$	$\left(\frac{2\pi}{3D_{max1}} + \frac{\pi^2}{3D_{max1}^2} + \frac{4}{3D_3} + \frac{4}{3D_3^2} \right) \left(1 - \frac{I_{peak(m)} I_{min(m)}}{(I_{peak} + I_{min})^2} \right) + \frac{0.8}{D_{max1}} \left(\frac{\pi}{2} + 1 \right) + 0.8 + \frac{0.8}{D_3} + \frac{I_{peak(m)}}{D_{max1} I_{Tav(m)}}$

As usual, the voltage gains of the power converters used in energy storage applications are different. This means that the duty cycle values and power loss values (P_{con}^*) are different depending on which way the power converters are used. For instance, a full-bridge converter, shown in Figure 9k, operates as a boost converter with duty cycle D_1 when energy is stored and as a buck converter with duty cycle D_2 when delivering energy to the power grid. The relationship between the parameters D_1 and D_2 is equal to:

$$D_2 = 1 - D_1. \quad (16)$$

Thus, power loss P_{con}^* estimation depends on the direction of energy transfer. As long as the same amount of energy is sent in both directions, the power loss weight formula is used with weight factor $w = 0.5$:

$$P_{con}^* = 0.5P_{con1}^*(D_1) + 0.5P_{con2}^*(D_2), \quad (17)$$

where P_{con1}^* is the power loss value for operation in energy storage mode with duty cycle D_1 , and P_{con2}^* is the power loss value for operation in delivering energy to the power grid with duty cycle D_2 .

In two-stage DC–AC energy storage applications, the first and second stages operate independently, so their operation is defined by four duty cycles, i.e., D_1, D_2 for the first stage and D_3, D_4 for the second stage. However, DC–DC two-stage applications always contain AC links that are used for electric isolation and soft-switching. Therefore, one of the stages always works in passive mode as a rectifier with the same duty cycle.

Derived results in Figures 16 and 17 make it clear that more effective applications are designed with basic half- and full-bridge topologies with improved dynamic loss. For DC–DC applications, there are cascaded and interleaved half-bridge topologies and 3L-NPC converters, whereas effective DC–AC applications are based on full-bridge, and full-bridge and half-bridge topologies.

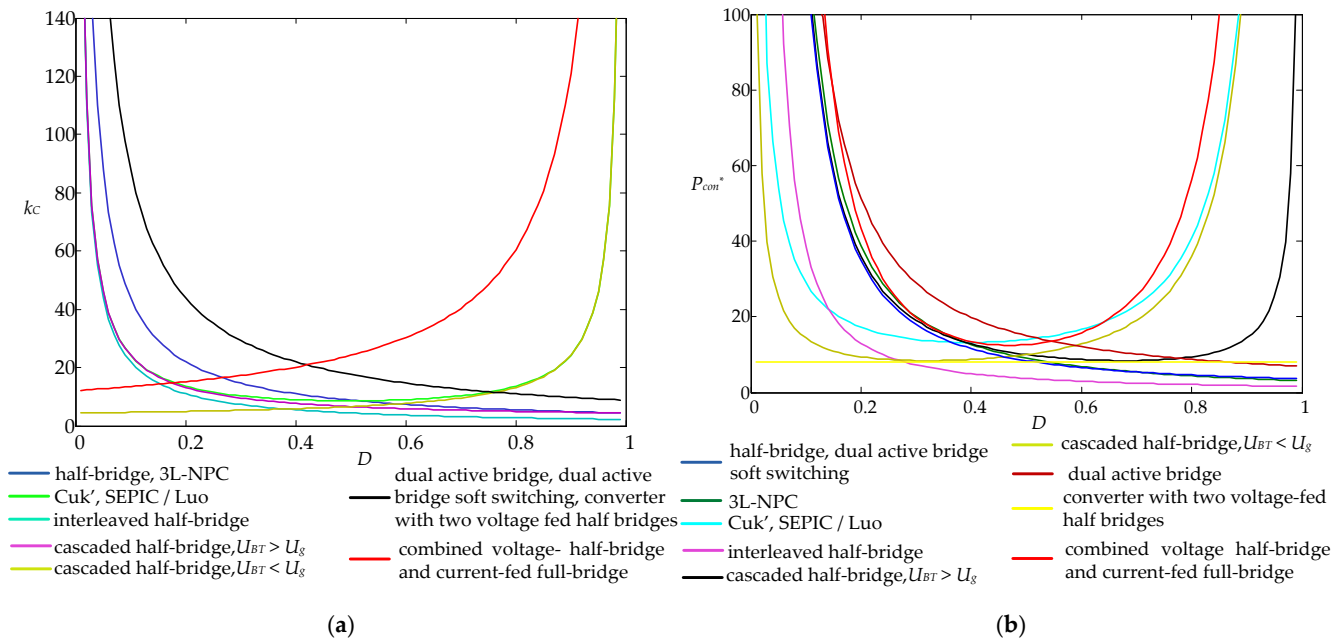


Figure 16. The cost factor k_C and normalized power loss P_{con}^* of DC–DC energy storage (a) Cost factor k_C ; (b) normalized power loss P_{con}^* in DC–DC energy storage converters.

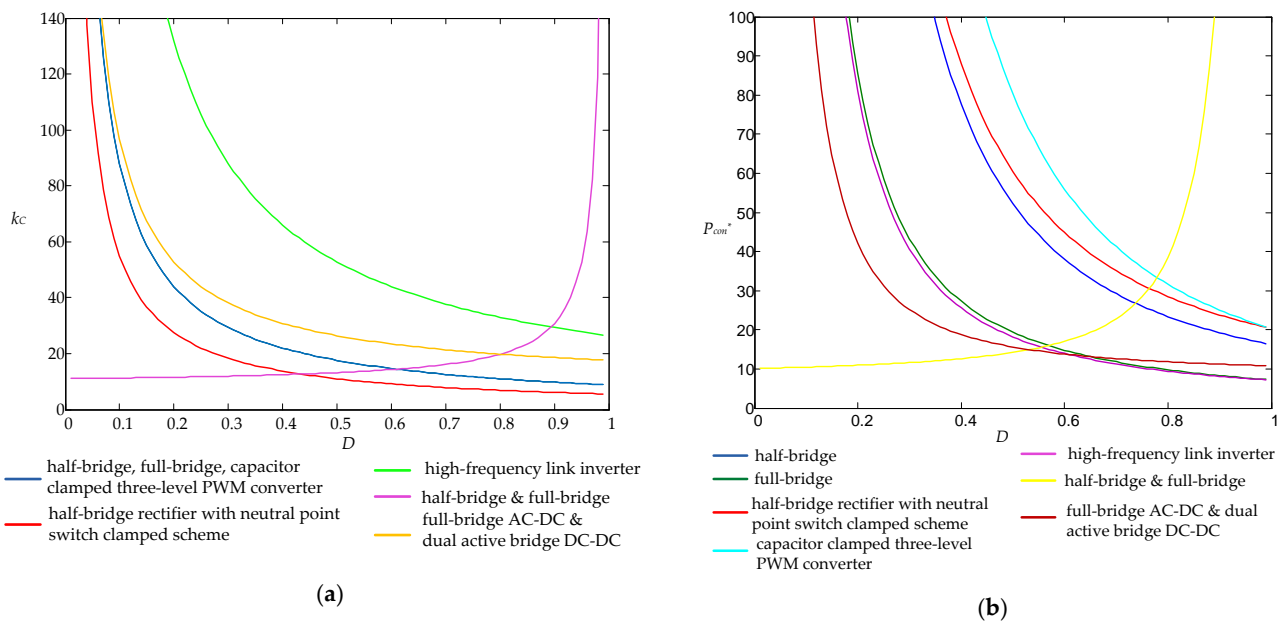


Figure 17. The parameters for DC–AC applications (a) Cost factor k_C ; (b) normalized power loss P_{con}^* in DC–AC energy storage converters.

Figure 16a,b show the cost factor k_C and normalized power loss P_{con}^* of DC–DC energy storage, while Figure 17a,b show the parameters for DC–AC applications.

5. High Voltage Gain Converters

Solar panels have relatively low voltage and current and are usually combined with batteries in parallel and series connections. The variation of power in solar radiation and in the parameters of the panels in the battery leads to a decrease in overall efficiency [87] and may cause system instability due to partial shadowing effects [88]. For mitigation of the foregoing drawbacks, high voltage gain converters are used. The common voltage boosting method, with a high-frequency transformer and high turns ratio n , increases

component stress on the secondary size and causes leakage inductance voltage spikes, thus non-isolated converters are often used in practice. A high gain value G for the conventional boost converter is achieved to the detriment of power loss with operation in modes with a close to unity duty cycle [89]. A cascading technique involves a series connection of several converters and expands the total voltage gain value G several times [90]. It increases the cost and complicates the converter design and control. For efficiency improvement the interleaving technique is used [91].

Other DC–DC converters, such as SEPIC and Flyback, can provide galvanic isolation via additional winding on the inductor core. These converters are used for high voltage gain but require additional snubber circuits to mitigate issues caused by leakage inductance [92] and usually suffer from increased transistor overvoltage with factors of 1.5–2.0. Passive dissipative RCD snubbers are commonly used [93], but for high-efficiency solutions more sophisticated active [94,95] or passive [96,97] regenerative snubbers deliver energy leakage inductance on the load or primary energy source. In addition, an isolated solution with leakage inductance allows the implementation of transistor soft-switching as well as voltage doubling, for instance, in an LC parallel current source converter with a voltage doubler [98]. The idea of capacitor voltage doubling is used for a set of multi-cell flying capacitor converters: super lift voltage converter [99], modified voltage lift converter [100], Cockcroft Walton multiplier based boost converter [101], Dickson multiplier based boost converter [101], boost derived MIESC SC-cell converter [102], and buck-boost derived MIESC SC-cell converter [102]. Capacitor voltage doubling is also realized in converters based on a three-state switching cell (3SSC) that is a combination of two switching PWM cells (2SSC) [103]. Such converters have reduced the size, weight, and volume of magnetics and reduced the current stress of switches.

Figure 18 shows the reviewed topologies of high gain converters, whereas Table 8 analyzes the main features of high gain converters, i.e., voltage gain G , switch voltage stress, and basic parameters k_C and P_{con}^* .

As shown in Figure 19a, an essential problem for high gain applications is significant transistor overvoltage. As a result, power converters with lower transistor stress recalculated on the gain unit, such as Cockcroft–Walton and Dickson multiplier-based boost converters, boost derived MIESC SC-cell converters, and boost 3SSC cell converters, are more appealing for high voltage application design.

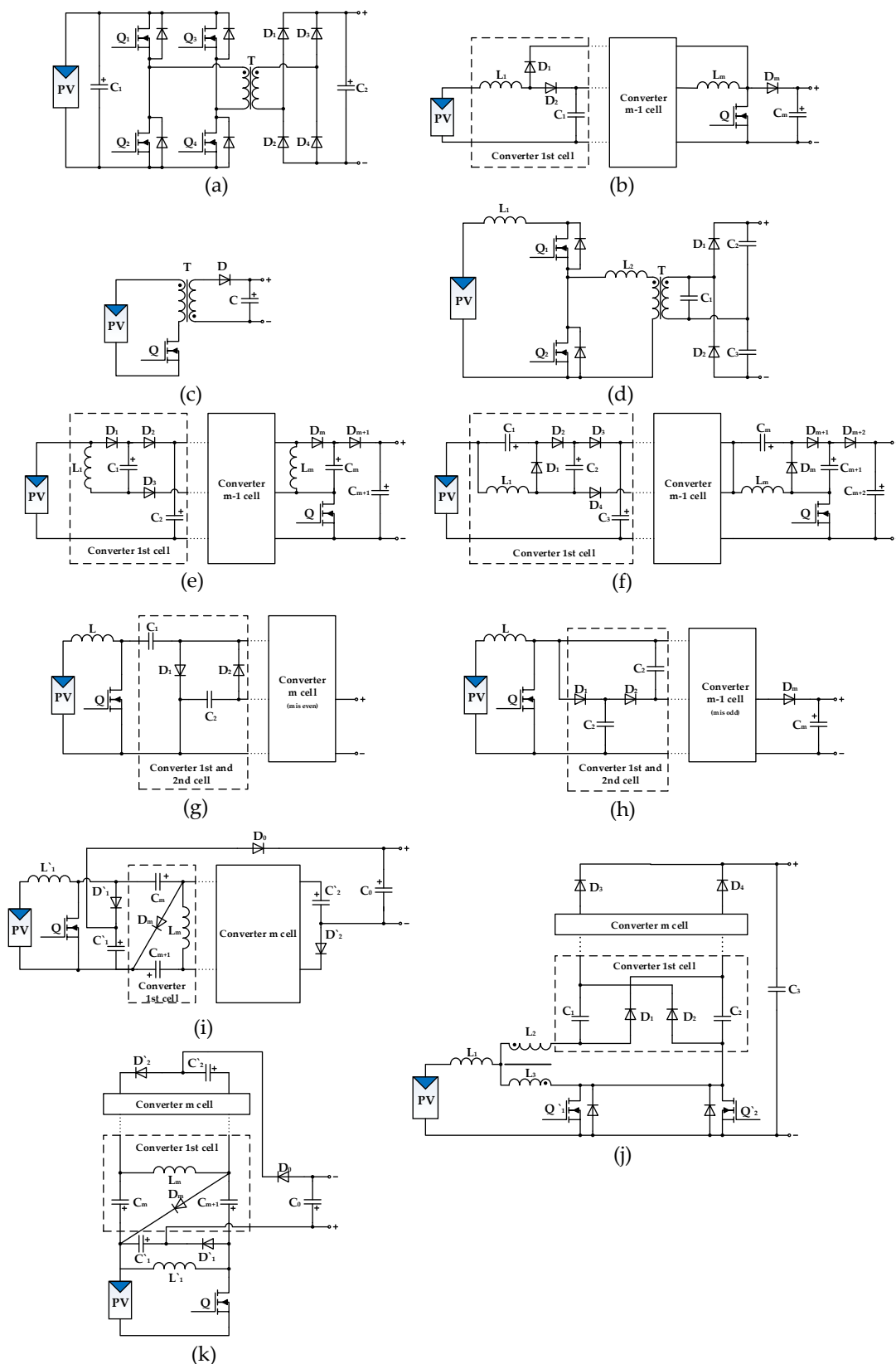


Figure 18. High voltage gain converters: (a) isolated full-bridge; (b) cascaded boost converter; (c) flyback; (d) LC parallel resonant converter with voltage doubler; (e) super lift voltage converter; (f) modified voltage lift converter; (g) Cockcroft–Walton multiplier based boost converter; (h) Dickson multiplier based boost converter; (i) boost derived MIESC SC-cell converter; (j) boost 3SSC cell converter; (k) buck-boost derived MIESC SC-cell converter.

Table 8. High voltage gain converters: comparative analysis.

Converter Topology	G	k _C	P _{con} *
Isolated full-bridge, Figure 18a	nD	$\frac{8I_{peak}}{DI_{Tav}}$	$\frac{32}{3D} \left(1 - \frac{I_{peak} I_{min}}{(I_{peak} + I_{min})^2} \right) + \frac{1.6}{D} + \frac{2I_{peak}}{DI_{Tav}}$
Conventional boost converter, Figure 9b	$\frac{1}{1-D}$	$\frac{I_{peak}}{(1-D)I_{Tav}}$	$\frac{4D}{3(1-D)^2} \left(1 - \frac{I_{peak} I_{min}}{(I_{peak} + I_{min})^2} \right) + 0.8 + \frac{I_{peak}}{(1-D)I_{Tav}}$
Cascaded boost converter [90], Figure 18b	$\frac{1}{(1-D)^2}$	$\frac{I_{peak}}{(1-D)^2 I_{Tav}}$	$\frac{4D}{3(1-D)^2} \left(1 - \frac{I_{peak} I_{min}}{(I_{peak} + I_{min})^2} \right) + \frac{0.8D^2}{(1-D)^2} + 0.8 + \frac{0.8}{1-D} + \frac{2I_{peak}}{(1-D)I_{Tav}}$
SEPIC [92], Figure 9d, Flyback [92], Figure 18c	$\frac{nD}{1-D}$	$\frac{1.5I_{peak}}{(1-D)I_{Tav}}$	$\frac{3}{D(1-D)^2} \left(1 - \frac{I_{peak} I_{min}}{(I_{peak} + I_{min})^2} \right) + \frac{0.8}{D} + \frac{I_{peak}}{(1-D)DI_{Tav}}$
LC parallel current source converter with voltage doubler [98], Figure 18d	$\frac{2n}{1-D}$	$\frac{1.1I_{peak}}{(1-D)I_{Tav}}$	$\left(\frac{2.42D}{3(1-D)^4} + \frac{8}{3(1-D)} \right) \left(1 - \frac{I_{peak} I_{min}}{(I_{peak} + I_{min})^2} \right) + 0.8 + \frac{I_{peak}}{(1-D)I_{Tav}}$
Super lift voltage converter [99], m cells, Figure 18e	$\left(\frac{2-D}{1-D} \right)^m$	$\left(\left(\frac{2-D}{1-D} \right)^m - 1 \right) \frac{I_{peak}}{I_{Tav}}$	$\frac{4D}{3(1-D)^2} \left(1 - \frac{I_{peak} I_{min}}{(I_{peak} + I_{min})^2} \right) + \frac{(1.6(m-1)+0.8)D}{(1-D)} + 0.8m + \frac{1.5mI_{peak}}{(1-D)I_{Tav}}$
Modified voltage lift converter [100], m cells, Figure 18f	$\left(\frac{2}{1-D} \right)^m$	$\left(\left(\frac{2}{1-D} \right)^m - 1 \right) \frac{I_{peak}}{I_{Tav}}$	$\frac{4D}{3(1-D)^2} \left(1 - \frac{I_{peak} I_{min}}{(I_{peak} + I_{min})^2} \right) + \frac{(1.6(m-1)+0.8)D}{(1-D)} + 1.6m + \frac{2mI_{peak}}{(1-D)I_{Tav}}$
Cockcroft–Walton and Dickson multiplier based boost converter [101], m cells, Figure 18g,h	$\frac{m+D}{1-D}$	$\frac{I_{peak}}{(1-D)I_{Tav}}$	$\frac{4D}{3(1-D)^2} \left(1 - \frac{I_{peak} I_{min}}{(I_{peak} + I_{min})^2} \right) + \frac{0.8mD}{(1-D)} + 0.8(m+1) + \frac{(m+0.5)I_{peak}}{(1-D)I_{Tav}}$
Boost derived MIESC SC-cell converter [102], m cells, Figure 18i	$\left(\frac{2}{1-D} \right)^m$	$\frac{I_{peak}}{(1-D)I_{Tav}}$	$\frac{4D}{3(1-D)^2} \left(1 - \frac{I_{peak} I_{min}}{(I_{peak} + I_{min})^2} \right) + \frac{0.8D}{(1-D)} + 0.8(m+2) + \frac{0.5(m+4)I_{peak}}{(1-D)I_{Tav}}$
Buck-boost derived MIESC SC-cell converter [102], m cells, Figure 18j	$\left(\frac{1+D}{1-D} \right)^m$	$\frac{I_{peak}}{D(1-D)I_{Tav}}$	$\frac{4}{3D(1-D)^2} \left(1 - \frac{I_{peak} I_{min}}{(I_{peak} + I_{min})^2} \right) + \frac{0.8}{1-D} + \frac{0.8(m+2)}{D} + \frac{0.5(m+4)I_{peak}}{(1-D)DI_{Tav}}$
Boost 3SSC cell converter [103], m cells, Figure 18k	$\frac{m+1}{1-D}$	$\frac{2I_{peak}}{(1-D)I_{Tav}}$	$\left(\frac{2D}{3(1-D)^2} + \frac{4}{3(1-D)} \right) \left(1 - \frac{I_{peak} I_{min}}{(I_{peak} + I_{min})^2} \right) + 1.6 + \frac{(m+0.5)I_{peak}}{(1-D)I_{Tav}}$

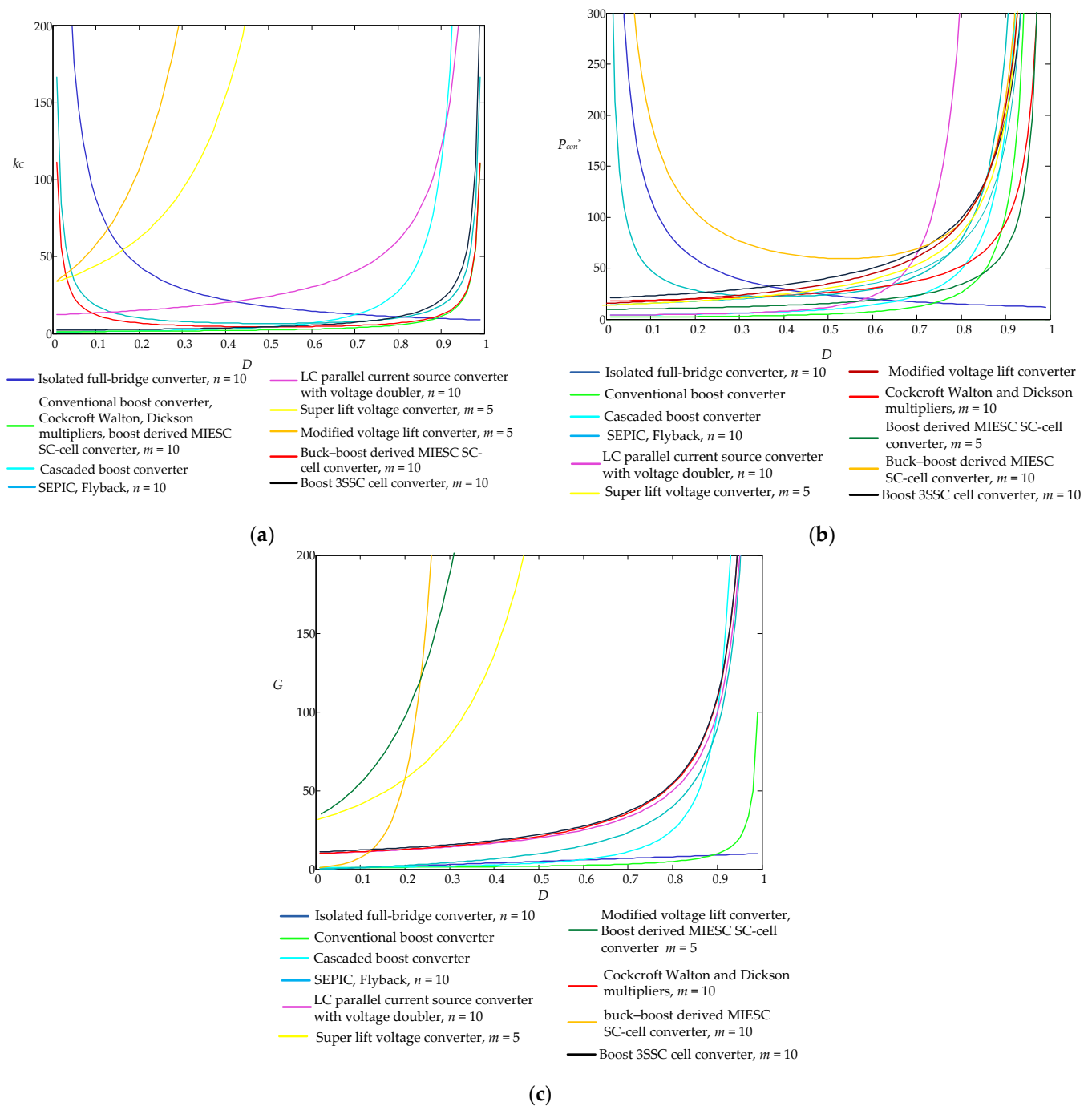


Figure 19. In high voltage gain converters: (a) cost factor k_C ; (b) normalized power loss P_{con}^* ; and (c) voltage gain G .

6. Hybrid PV Applications

Hybrid PV systems are complex solutions that include multiple energy sources, such as a diesel generator [104], a wind turbine or a fuel cell [105]; integrated energy storage with an interruptible power supply function; and multiple AC and/or DC outputs. The system is often used for standalone applications for reliable power supply [106] or as an advanced uninterruptable power system that allows generating or consuming energy from the grid for imbalance elimination of PV systems and load [107]. The hybrid system consists of several stages which, in the common case, are realized with individual power converters, which is the redundant solution. Combining identical converter links makes it possible to reduce the number of elements in the system and simplify control [108]. The simplest case is the use of

multi-winding transformers [109]. In non-isolated applications, combinations of cells with boost, buck, and buck-boost converters with unidirectional [110] or bidirectional [111–113] energy flow are implemented. For distributed systems, interleaved multi-input solutions are also used [114].

As usual, multi-port solutions are designed for DC–DC [115] or DC–AC [116–119] applications with renewable sources and energy storage suitable for PV and wind applications as well. Table 9 lists the analytical expressions of the multiport converter parameters shown in Figure 20.

Table 9. A comparative analysis of the effectiveness of the hybrid converter.

Converter Topology	k_C	P_{con}^*
Boost three-port converter [110], Figure 20a	$\frac{3}{1-D} \frac{I_{peak}}{I_{Tav}}$	$\frac{16D}{9(1-D)^2} \left(1 - \frac{I_{peak} I_{min}}{(I_{peak} + I_{min})^2}\right) + 0.8 + \frac{I_{peak}}{(1-D)I_{Tav}}$
Buck three-port converter [110], Figure 20b	$\left(\frac{2}{D} + 1\right) \frac{I_{peak}}{I_{Tav}}$	$\frac{4}{3D} \left(1 - \frac{I_{peak} I_{min}}{(I_{peak} + I_{min})^2}\right) \left(1 + \frac{1}{3D}\right) + \frac{0.8(1.33-D)}{D} + \frac{I_{peak}}{DI_{Tav}}$
Buck-boost three-port converter [110], Figure 20c	$\frac{2}{D(1-D)} \frac{I_{peak}}{I_{Tav}}$	$\frac{4}{3} \left(\frac{1}{D(1-D)^2} + \frac{1}{3(1-D)}\right) \left(1 - \frac{I_{peak} I_{min}}{(I_{peak} + I_{min})^2}\right) + \frac{0.8}{D} - \frac{0.8}{3} + \frac{I_{peak}}{3I_{Tav}} \left(\frac{2}{D(1-D)} + \frac{1}{D}\right)$
Bidirectional buck-boost converter [111], Figure 20d	$\frac{8I_{peak}}{DI_{Tav}}$	$\frac{4D}{(1-D)^2} \left(1 - \frac{I_{peak} I_{min}}{(I_{peak} + I_{min})^2}\right) + \frac{0.8 \cdot (1-D)}{3D} + \frac{3.2}{3} + \frac{0.5I_{peak}}{3DI_{Tav}}$
Switched capacitor multi-port converter [112], Figure 20e	$\frac{2I_{peak}}{DI_{Tav}}$	$\frac{1}{3D} \left(1 - \frac{I_{peak} I_{min}}{(I_{peak} + I_{min})^2}\right) + \frac{5 \cdot 0.8(1-D)}{3D}$
Dual active bridge multi-port converter [112], Figure 20f	$\frac{4I_{peak}}{DI_{Tav}}$	$\left(\frac{4}{9D} + \frac{8D}{9(1-D)^2} \left(1 + \frac{1}{2D}\right)\right) \left(1 - \frac{I_{peak} I_{min}}{(I_{peak} + I_{min})^2}\right) + \frac{0.8}{3D} + \frac{1.6}{3} + \frac{0.8D}{3(1-D)} + \frac{I_{peak}}{3DI_{Tav}}$
Double-stage with battery boost converter [116], Figure 20g	$\frac{I_{peak}}{I_{Tav}} \left(\frac{3}{1-D} + 8\right)$	$\left(\frac{4D}{3(1-D)^2} + \frac{\pi}{3} + \frac{\pi^2}{6}\right) \left(1 - \frac{I_{peak} I_{min}}{(I_{peak} + I_{min})^2}\right) + 0.8 + 0.4 \left(\frac{\pi}{2} + 1\right) + \frac{0.5I_{peak}}{I_{Tav}(1-D)} + \frac{0.5I_{peak}}{I_{Tav}}$
Fully soft-switched multi-port DC-DC converter [113], Figure 20h	$\frac{5I_{peak}}{DI_{Tav}}$	$\frac{4}{9} \left(\frac{1}{D^2} + \frac{D+1}{(1-D)^2}\right) \left(1 - \frac{I_{peak} I_{min}}{(I_{peak} + I_{min})^2}\right) + \frac{0.8(1-D)}{3D}$
Multiple-input SEPIC converter, m cells [114], Figure 20i	$\frac{I_{peak}}{D(1-D)I_{Tav}}$	$\frac{4}{3Dm(1-D)^2} \left(1 - \frac{I_{peak} I_{min}}{(I_{peak} + I_{min})^2}\right) + \frac{0.8}{D} + \frac{0.8}{1-D} + \frac{1.5I_{peak}}{I_{Tav}mD(1-D)}$
NPC multiport converter [110], Figure 20j	$\frac{8I_{peak}}{D_{max}I_{Tav}}$	$\left(\frac{2\pi}{9D_{max}} + \frac{\pi^2}{9D_{max}^2}\right) \left(1 - \frac{I_{peak} I_{min}}{(I_{peak} + I_{min})^2}\right) + \frac{0.8}{D_{max}} \left(\frac{\pi}{2} + 1\right) + \frac{I_{peak}}{D_{max}I_{Tav}}$



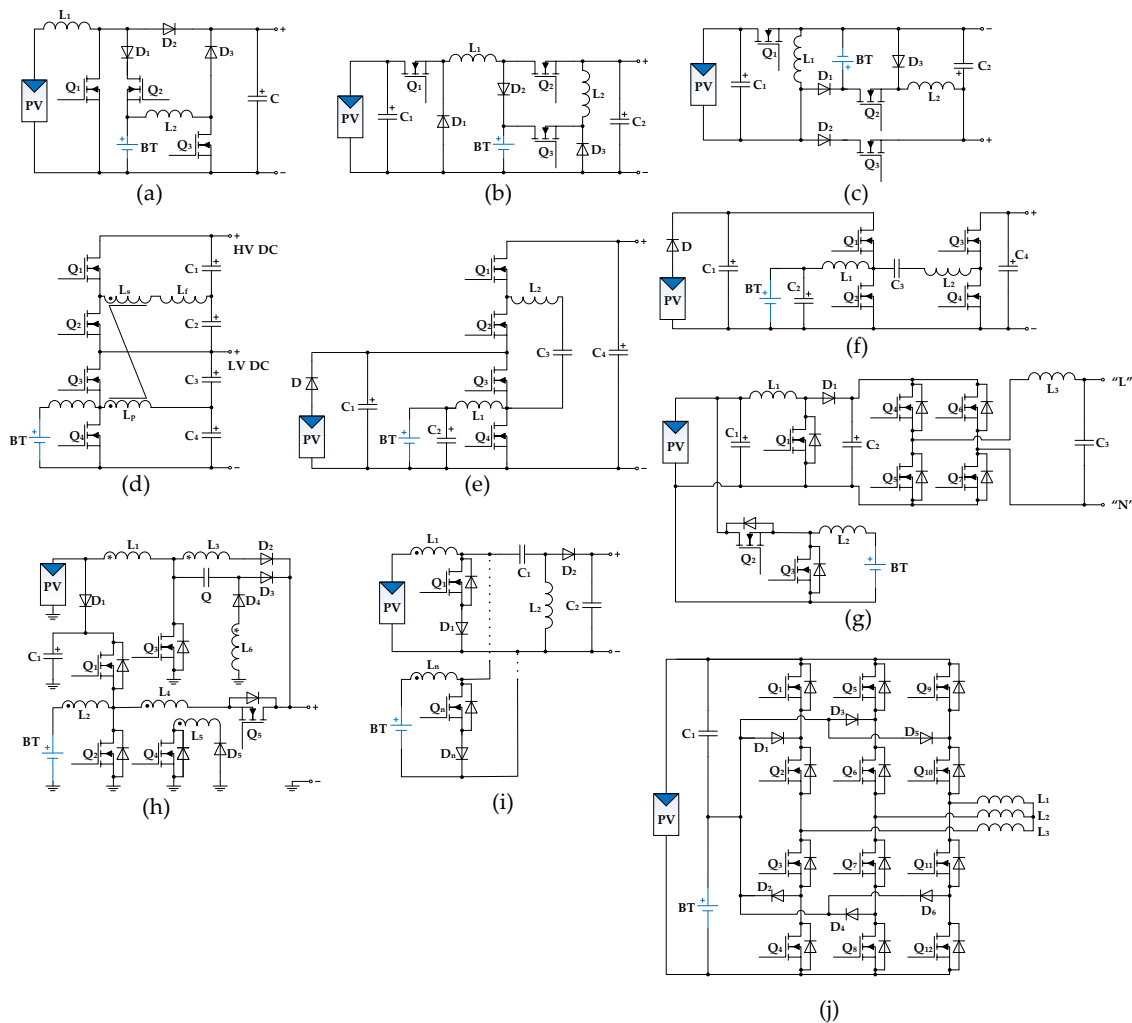


Figure 20. Hybrid converters: (a) boost three-port converter; (b) buck three-port converter; (c) buck-boost three-port converter; (d) bidirectional buck-boost converter; (e) switched capacitor multi-port converter; (f) dual active bridge multi-port converter; (g) double-stage with battery boost converter; (h) fully soft-switched multi-port DC–DC converter; (i) multiple-input SEPIC converter; (j) NPC multiport converter.

Hybrid converter parameters k_C and P_{con}^* are shown in Figure 21a,b, respectively.

As shown in Figure 21, the lowest values of k_C and P_{con}^* parameters are achieved for converters with basic buck and boost topologies, as well as for more complex switched-capacitor multi-port converters and dual active bridge multi-port converters with soft-switching transistor commutation. However, the analyzed hybrid converters generally have the same number of transistors as common power converters with the same features. The hybrid converters, on the other hand, have about the same power loss and cost as their counterparts with common topologies.

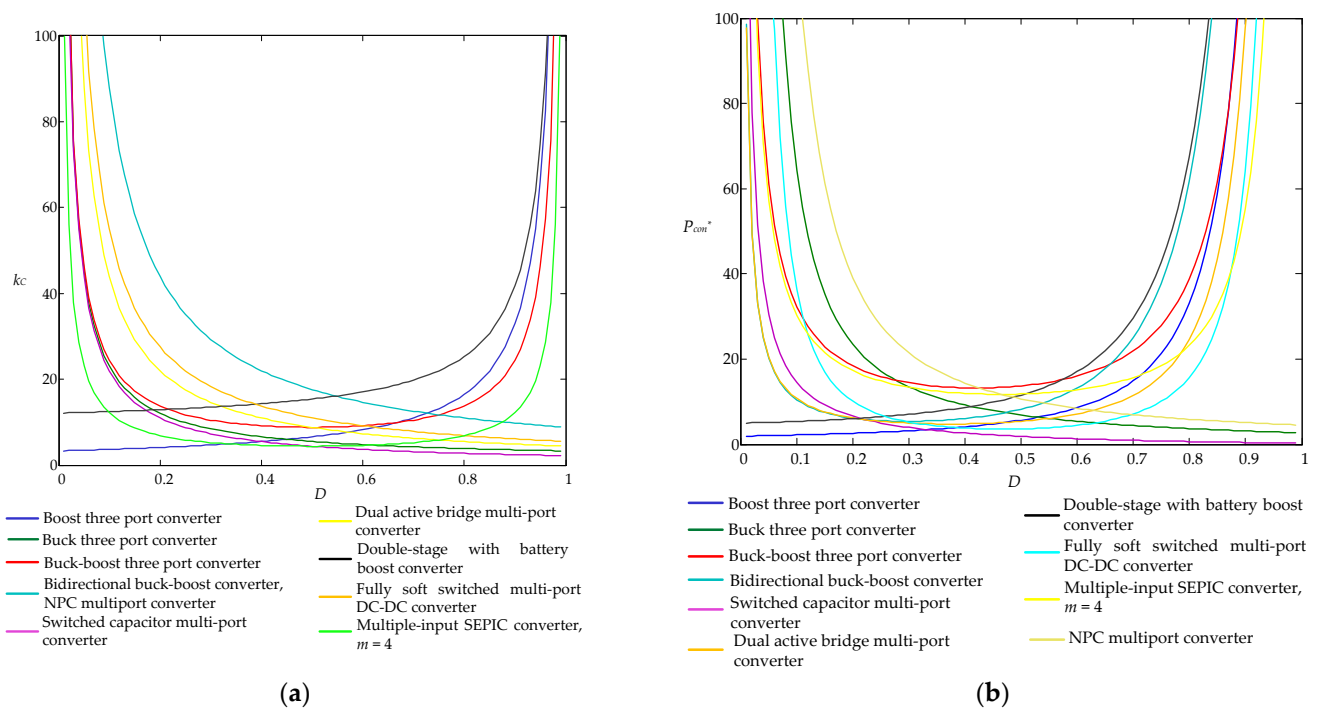


Figure 21. Hybrid converter parameters: (a) cost factor k_c ; (b) normalized power loss P_{con}^* .

7. Discussion

Derived analytical expressions for cost k_c and power loss P_{con}^* factors are evaluation indicators for selecting the converter topology for PV application design based on duty cycle D . Such parameter representations are strictly related to the converter operation mode and help to define the duty cycle D range of the PV application. However, the comparative analysis of the converter based on k_c and P_{con}^* factors as functions of D , $k_c = f(D)$, and $P_{con}^* = f(D)$, is inconvenient due to their different voltage gains. This is especially true when comparing different types of converters, i.e., buck, boost, and buck-boost converters. It is more informative to analyze parameters k_c and P_{con}^* in some load voltage ranges ($U_{L(\min)}$, $U_{L(\max)}$) where the PV application operates for comparative analysis unification. If voltage $U_{L(\min)}$ is associated with voltage gain G_{\min} and voltage $U_{L(\max)}$ with voltage gain G_{\max} , we can define the maximum gain factor G_{\max}^* :

$$G_{\max}^* = \frac{G_{\max}}{G_{\min}}. \tag{18}$$

The real gain factor G^* of a converter is always varied in the range $[1, G_{\max}^*]$ and may be used as a universal parameter for comparing different types of power converters.

Due to the opportunity to achieve gain factor G_{\max}^* on different duty cycle D ranges $[D_{\min}; D_{\max}]$, the range is defined according to providing the lowest cost and/or power loss. According to the specified conditions and obtained results:

- In buck converters, the output voltage maximum value $U_{L(\max)}$ is fixed to the input voltage U_{in} , $U_{L(\max)} = U_{in}$ that corresponds to $D_{\max} = 1$;
- In boost converters, the output voltage minimum value $U_{L(\min)}$ is fixed to the input voltage U_{in} , $U_{L(\min)} = U_{in}$ that corresponds to $D_{\min} = 0$;
- In buck-boost converters, the lowest values of k_c and P_{con}^* are achieved in the middle of the duty cycle range, $D = 0.5$. Therefore, for the proper definition of $D_{\min} < 0.5$ and $D_{\max} > 0.5$, one of the following equations is solved:

$$\begin{aligned}
 k_C(D_{\min}) &= k_C(D_{\max}); \\
 &\text{or} \\
 P_{con}^*(D_{\min}) &= P_{con}^*(D_{\max}),
 \end{aligned}
 \tag{19}$$

The values of $U_{L(\min)} = f(D_{\min})$ and $U_{L(\max)} = f(D_{\max})$ are defined depending on the choice of minimization parameter.

After the proposed transformation, parameters k_C and P_{con}^* may be defined based on a function of the parameter G^* that varies in the range $[1, G_{\max}^*]$. Due to this representation, a comprehensive comparison analysis of converters for the defined value of parameter G^* may be conducted. However, in real PV applications, because of variations in solar insolation, temperature, battery state of charge, grid voltage, etc., the gain parameter G^* varies in range of $1 \dots G_{\max}^*$, and the parameters k_C and P_{con}^* change, respectively. The cost factor k_C of the PV application is obviously defined by the largest value of G_{\max}^* , whereas the power loss parameter P_{con}^* is defined as an intermediate mean value $P_{con(av)}^*$ between $P_{con}^*(\min) = f(G^* = 1)$ and $P_{con}^*(\max) = f(G^* = G_{\max}^*)$. The precise $P_{con(av)}^*$ value is determined by a weighted function that defines a probability distribution law of G^* , $p(G^*)$, with values ranging from 1 to G_{\max}^* [120]:

$$P_{con(av)}^* = \int_1^{G_{\max}^*} p(G^*) \cdot P_{con}^*(G^*) dG^*.
 \tag{20}$$

For example, in the case of a continuous uniform distribution, $p = 1/(G_{\max}^* - 1)$ [121] Formula (20) yields:

$$P_{con(av)}^* = \frac{1}{G_{\max}^* - 1} \int_1^{G_{\max}^*} P_{con}^*(G^*) dG^*.
 \tag{21}$$

Additionally, analytical expressions of converter efficiency parameters k_C and $P_{con(av)}^*$ for DC–DC converters listed in Table 3 in space of the variable G^* are shown in Table 10 and illustrated in Figure 22a,b, respectively.

A representation of the parameters k_C and $P_{con(av)}^*$ with the gain factor G^* aids in the estimation of converter features within a given voltage range, as well as the comparison of different converter types (buck, boost and buck-boost). For example, a buck converter has the lowest cost factor k_C value for $G^* \in (1; 4.5)$, whereas a buck-boost converter is preferable for $G^* \in (4.5; \infty)$ applications. A similar decision may be made for mean power loss $P_{con(av)}^*$, which has the lowest value for buck converter modifications in all G^* ranges.

Obviously, for different models of semiconductor devices and other probability distribution laws, the results would be different. This allows you to compare power converters based on the PV application's start-up conditions.

Table 10. Comparative analysis of the DC–DC converter’s effectiveness in space of the variable G^* .

Converter Topology	k_C	$P_{con(av)}^*$
Buck	$\frac{G_{max}^* I_{peak}}{I_{Tav}}$	$\frac{1}{G_{max}^* - 1} \left(\frac{G_{max}^{*2} - 1}{2} \left(\frac{4}{3} \left(1 - \frac{I_{peak} I_{min}}{(I_{peak} + I_{min})^2} \right) + 0.8 + \frac{I_{peak}}{I_{Tav}} \right) - 0.8(G_{max}^* - 1) \right)$
Boost	$\frac{G_{max}^* I_{peak}}{I_{Tav}}$	
Buck-boost, SEPIC, Cuk'	$\frac{(1 + \sqrt{G_{max}^*})^2 I_{peak}}{\sqrt{G_{max}^*} I_{Tav}}$	$\frac{1}{G_{max}^* - 1} \left(\left(\frac{4(G_{max}^{*3} - 1)}{9} - \frac{2(G_{max}^{*2} - 1)}{3} \right) \left(1 - \frac{I_{peak} I_{min}}{(I_{peak} + I_{min})^2} \right) + 0.8(G_{max}^* - 1) + \frac{(G_{max}^{*2} - 1) I_{peak}}{2 I_{Tav}} \right) \times \frac{1}{G_{max}^* - 1} \left(\left(\frac{4}{3} \left(1 - \frac{I_{peak} I_{min}}{(I_{peak} + I_{min})^2} \right) + \frac{I_{peak}}{I_{Tav}} \right) \times \left(\frac{2}{3} (G_{max}^*)^{3/4} + 3(G_{max}^*)^{1/2} + 6(G_{max}^*)^{1/4} + \frac{1}{2} \ln(G_{max}^*) - \frac{29}{3} \right) + 0.8 \left((G_{max}^*)^{1/2} - 1 \right) + 0.53 \left((G_{max}^*)^{3/4} - 1 \right) + 1.6 \left((G_{max}^*)^{1/2} - (G_{max}^*)^{1/4} \right) + 0.8 \left(G_{max}^* - (G_{max}^*)^{1/2} \right) + \left(\frac{4}{3} \left(1 - \frac{I_{peak} I_{min}}{(I_{peak} + I_{min})^2} \right) + \frac{I_{peak}}{I_{Tav}} \right) \times \left(2 \left((G_{max}^*)^{3/2} - (G_{max}^*)^{3/4} \right) + \frac{1}{2} (G_{max}^{*2} - G_{max}^*) \right) + 2 \left((G_{max}^*)^{1/2} - (G_{max}^*)^{1/4} \right) + 3 \left(G_{max}^* - (G_{max}^*)^{1/2} \right) \right)$
Soft-switching buck	$\frac{2G_{max}^* I_{peak}}{I_{Tav}}$	$\frac{1}{G_{max}^* - 1} \left(\frac{G_{max}^{*2} - 1}{2} \left(\frac{4}{3} \left(1 - \frac{I_{peak} I_{min}}{(I_{peak} + I_{min})^2} \right) + 0.8 \right) - 0.8(G_{max}^* - 1) \right)$
Soft-switching boost	$\frac{2G_{max}^* I_{peak}}{I_{Tav}}$	$\frac{1}{G_{max}^* - 1} \left(\left(\frac{4(G_{max}^{*3} - 1)}{9} - \frac{2(G_{max}^{*2} - 1)}{3} \right) \left(1 - \frac{I_{peak} I_{min}}{(I_{peak} + I_{min})^2} \right) + 0.8(G_{max}^* - 1) \right)$
Interleaved buck	$\frac{G_{max}^* I_{peak}}{I_{Tav}}$	$\frac{1}{G_{max}^* - 1} \times \left(\frac{G_{max}^{*2} - 1}{2} \left(\frac{4}{3m} \left(1 - \frac{I_{peak} I_{min}}{(I_{peak} + I_{min})^2} \right) + 0.8 + \frac{I_{peak}}{m I_{Tav}} \right) - 0.8(G_{max}^* - 1) \right)$
Interleaved boost	$\frac{G_{max}^* I_{peak}}{I_{Tav}}$	$\frac{1}{G_{max}^* - 1} \left(\frac{1}{m} \left(\frac{4(G_{max}^{*3} - 1)}{9} - \frac{2(G_{max}^{*2} - 1)}{3} \right) \left(1 - \frac{I_{peak} I_{min}}{(I_{peak} + I_{min})^2} \right) + 0.8(G_{max}^* - 1) + \frac{(G_{max}^{*2} - 1) I_{peak}}{2m I_{Tav}} \right)$

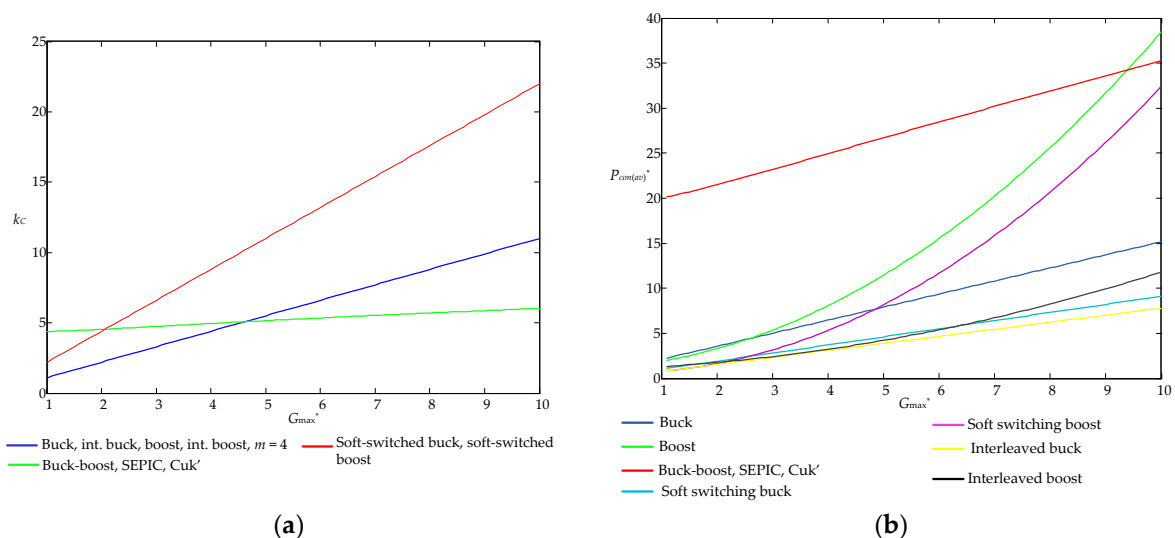


Figure 22. Comparative analysis of the DC–DC converter’s effectiveness in space of the variable G^* : (a) cost factor k_C ; (b) normalized mean power loss $P_{con(av)}^*$.

8. Conclusions

Industrial PV solutions contain different kinds of applications designed with power converters as electric energy transformers and interconnectors. Thus, the specific converter requirements vary depending on the application which complicates the selection of the appropriate type of converter for a specific task. The paper highlights generalized

criteria that have a critical impact on the efficiency and cost of converter topologies for PV applications that allows performing a comparative analysis in space of two numerical parameters, namely cost and power loss factors, of common PV applications, i.e., grid-on, energy storage, hybrid, and high voltage gain, based on cost and power loss factors.

According to the results of the analysis, the following conclusions are made:

- Basic DC–DC buck and boost topologies, as well as full-bridge topologies for DC–AC applications, have lower cost and power loss factors, whereas more complex interleaved or soft-switching topologies may decrease power loss by increasing the converter total cost;
- For DC–AC applications with a low or medium voltage range, it is advisable to use single-stage DC–AC converters, whereas for wide voltage range applications, two-stage converters have better cost and power loss factors;
- High voltage gain applications suffer from high transistor voltage stress. Therefore, specialized power converter topologies with reduced voltage stress, such as Cockcroft–Walton and Dickson multiplier-based boost converters, boost derived MIESC SC-cell converters, and boost 3SSC cell converters, have the advantage over their counterparts;
- Hybrid converters have approximately the same power loss and cost as power converters with common topologies because of the same number of power transistors;
- For clear analysis of different types of converters, it is better to represent cost and power loss factors in the space of gain factor and analyze the impact of the environment on gain factor probability distribution during operation.

Author Contributions: Conceptualization, I.V.; Formal analysis, I.V. and M.L.; Validation, I.V. and M.L.; Methodology, I.V.; Visualization, M.L. and K.N.; Investigation, M.L., K.N., and B.P.; Writing — original draft, K.N. and B.P.; Resources, O.H.; Writing—review and editing, B.P. and O.H.; Supervision, R.M.S. and O.H.; Project administration, R.M.S.; Funding acquisition, R.M.S. All authors have read and agreed to the published version of the manuscript.

Funding: This research was funded by the EU Horizon 2020 Framework Programme Project: 955614—SMARTGYsum—H2020-MSCA-ITN-2020.

Institutional Review Board Statement: Not applicable.

Informed Consent Statement: Not applicable.

Data Availability Statement: Not applicable.

Conflicts of Interest: The authors declare no conflict of interest.

References

1. Qazi, A.; Hussain, F.; Rahim, N.A.; Hardaker, G.; Alghazzawi, D.; Shaban, K.; Haruna, K. Towards Sustainable Energy: A Systematic Review of Renewable Energy Sources, Technologies, and Public Opinions. *IEEE Access* **2019**, *7*, 63837–63851. [CrossRef]
2. Statistical Review of World Energy 2021, 70th ed. Available online: <https://www.bp.com/content/dam/bp/business-sites/en/global/corporate/pdfs/energy-economics/statistical-review/bp-stats-review-2021-full-report.pdf> (accessed on 30 August 2021).
3. Shubbak, M.H. Advances in solar photovoltaics: Technology review and patent trends. *Renew. Sustain. Energy Rev.* **2019**, *115*, 109383. [CrossRef]
4. Mehra, V.; Amatya, R.; Ram, R.J. Estimating the value of demand-side management in low-cost, solar micro-grids. *Energy* **2018**, *163*, 74–87. [CrossRef]
5. Romashko, V.J.; Verbitsky, I.V.; Kyrychik, I.I. Energy losses analyze in solar battery maximum power picking system. *Tech. Electrodyn.* **2014**, *4*, 55–57.
6. Clauser, C.; Ewert, M. The renewables cost challenge: Levelized cost of geothermal electric energy compared to other sources of primary energy—Review and case study. *Renew. Sustain. Energy Rev.* **2018**, *82*, 3683–3693. [CrossRef]
7. Tummuru, N.R.; Mishra, M.K.; Srinivas, S. Integration of PV/battery hybrid energy conversion system to the grid with power quality improvement features. In Proceedings of the IEEE International Conference on Industrial Technology (ICIT), Cape Town, South Africa, 25–28 February 2013. [CrossRef]
8. Hua, C.-C.; Fang, Y.-H.; Wong, C.-J. Improved solar system with maximum power point tracking. *IET Renew. Power Gener.* **2018**, *12*, 806–814. [CrossRef]

9. Darvishzadeh, P.; Redzwan, G.; Ahmadi, R.; Gorji, N.E. Modeling the degradation/recovery of short-circuit current density in perovskite and thin film photovoltaics. *Org. Electron.* **2017**, *43*, 247–252. [[CrossRef](#)]
10. Hussaian Basha, C.H.; Rani, C. Performance Analysis of MPPT Techniques for Dynamic Irradiation Condition of Solar PV. *Int. J. Fuzzy Syst.* **2020**, *22*, 2577–2598. [[CrossRef](#)]
11. Zhuo, S.; Gaillard, A.; Li, Q.; MA, R.; Paire, D.; Gao, F. Current Ripple Optimization of Four-Phase Floating Interleaved DC-DC Boost Converter under Switch Fault. *IEEE Trans. Ind. Appl.* **2020**, *56*, 4214–4224. [[CrossRef](#)]
12. Raghavendra, K.V.G.; Zeb, K.; Muthusamy, A.; Krishna, T.N.V.; Kumar, S.V.S.V.P.; Kim, D.-H.; Kim, M.-S.; Cho, H.-G.; Kim, H.-J. A Comprehensive Review of DC–DC Converter Topologies and Modulation Strategies with Recent Advances in Solar Photovoltaic Systems. *Electronics* **2020**, *9*, 31. [[CrossRef](#)]
13. Vinnikov, D.; Chub, A.; Korkh, O.; Liivik, E.; Blaabjerg, F.; Kouro, S. MPPT performance enhancement of low-cost PV microconverters. *Sol. Energy* **2019**, *187*, 156–166. [[CrossRef](#)]
14. Kolsi, S.; Samet, H.; Amar, M.B. Design Analysis of DC-DC Converters Connected to a Photovoltaic Generator and Controlled by MPPT for Optimal Energy Transfer throughout a Clear Day. *J. Power Energy Eng.* **2014**, *2*, 27–34. [[CrossRef](#)]
15. Bukar, A.L.; Tan, C.W.A. Review on Stand-alone Photovoltaic-Wind Energy System with Fuel Cell: System Optimization and Energy Management Strategy. *J. Clean. Prod.* **2019**, *221*, 73–88. [[CrossRef](#)]
16. Bonkile, M.P.; Ramadesigan, V. Power management control strategy using physics-based battery models in standalone PV-battery hybrid systems. *J. Energy Storage* **2019**, *23*, 258–268. [[CrossRef](#)]
17. Kumar, A.; Gupta, N.; Gupta, V. A Comprehensive Review on Grid-Tied Solar Photovoltaic System. *J. Green Eng.* **2017**, *7*, 213–254. [[CrossRef](#)]
18. Ali Khan, M.Y.; Liu, H.; Yang, Z.; Yuan, X. A Comprehensive Review on Grid Connected Photovoltaic Inverters, Their Modulation Techniques, and Control Strategies. *Energies* **2020**, *13*, 4185. [[CrossRef](#)]
19. Mahmood, H.; Michaelson, D.; Jiang, J. A Power Management Strategy for PV/Battery Hybrid Systems in Islanded Microgrids. *IEEE J. Emerg. Sel. Top. Power Electron.* **2014**, *2*, 870–882. [[CrossRef](#)]
20. Mira, M.C.; Zhang, Z.; Knott, A.; Andersen, M.A.E. Analysis, Design, Modeling, and Control of an Interleaved-Boost Full-Bridge Three-Port Converter for Hybrid Renewable Energy Systems. *IEEE Trans. Power Electron.* **2017**, *32*, 1138–1155. [[CrossRef](#)]
21. Bhattacharjee, A.; Samanta, H.; Banerjee, N.; Saha, H. Development and validation of a real-time flow control integrated MPPT charger for solar PV applications of vanadium redox flow battery. *Energy Convers. Manag.* **2018**, *171*, 1449–1462. [[CrossRef](#)]
22. El Aroudi, A.; Haroun, R.; Al-Numay, M.; Huang, M. Multiple-Loop Control Design for a Single-Stage PV-Fed Grid-Tied Differential Boost Inverter. *Appl. Sci.* **2020**, *10*, 4808. [[CrossRef](#)]
23. Nassary, M.; Orabi, M.; Ghoneima, M.; El-Nemr, M.K. Single-Phase Isolated Bidirectional AC-DC Battery Charger for Electric Vehicle—Review. In Proceedings of the International Conference on Innovative Trends in Computer Engineering (ITCE), Aswan, Egypt, 2–4 February 2019. [[CrossRef](#)]
24. Sultana, W.R.; Sahoo, S.K.; Sukchai, S.; Yamuna, S.; Venkatesh, D. A review on state of art development of model predictive control for renewable energy applications. *Renew. Sustain. Energy Rev.* **2017**, *76*, 391–406. [[CrossRef](#)]
25. Deng, W.; Pei, W.; Li, N.; Zhang, G.; Ding, L.; Kong, L. AC/DC Hybrid Renewable Energy System Coordinated Control and Test Platform. In Proceedings of the 2021 3rd Asia Energy and Electrical Engineering Symposium (AEEES), Chengdu, China, 26–29 March 2021. [[CrossRef](#)]
26. Amir, A.; Amir, A.; Che, H.S.; El Khateb, A.; Rahim, N.A. Comparative Analysis of High Voltage Gain DC-DC Converter Topologies for Photovoltaic Systems. *Renew. Energy* **2018**, *136*, 1147–1163. [[CrossRef](#)]
27. Rahman, S.; Khan, I.; Rahman, K.; Al Otaibi, S.; Alkhamash, H.I.; Iqbal, A. Scalable Multiport Converter Structure for Easy Grid Integration of Alternate Energy Sources for Generation of Isolated Voltage Sources for MMC. *Electronics* **2021**, *10*, 1779. [[CrossRef](#)]
28. Chen, G.; Liu, Y.; Qing, X.; Wang, F. Synthesis of Integrated Multi-Port DC-DC Converters with Reduced Switches. *IEEE Trans. Ind. Electron.* **2019**, *67*, 4536–4546. [[CrossRef](#)]
29. Başoğlu, M.E.; Çakır, B. Comparisons of MPPT performances of isolated and non-isolated DC–DC converters by using a new approach. *Renew. Sustain. Energy Rev.* **2016**, *60*, 1100–1113. [[CrossRef](#)]
30. Gorji, S.A.; Sahebi, H.G.; Ektesabi, M.; Rad, A.B. Topologies and Control Schemes of Bidirectional DC–DC Power Converters: An Overview. *IEEE Access* **2019**, *7*, 117997–118019. [[CrossRef](#)]
31. Moghassemi, A.; Padmanaban, S. Dynamic Voltage Restorer (DVR): A Comprehensive Review of Topologies, Power Converters, Control Methods, and Modified Configurations. *Energies* **2020**, *13*, 4152. [[CrossRef](#)]
32. Ansari, S.; Chandel, A.; Tariq, M. A Comprehensive Review on Power Converters Control and Control Strategies of AC/DC Microgrid. *IEEE Access* **2020**, *9*, 17998–18015. [[CrossRef](#)]
33. Undeland, M.N.; Robbins, W.P.; Mohan, N. Power Electronics. In *Converters, Applications, and Design*, 3rd ed.; John Wiley & Sons: Hoboken, NJ, USA, 1995.
34. Ha, K.; Lee, C.; Kim, J.; Krishnan, R.; Oh, S.G. Design and development of brushless variable speed motor drive for low cost and high efficiency. *Proc. IAS Conf.* **2006**, *4*, 1649–1656. [[CrossRef](#)]
35. IEC 61730-1; Photovoltaic (PV) Module Safety Qualification-Part 1: Requirements for Construction. CENELEC: Brussels, Belgium, 2018.
36. IEC 61730-2; Photovoltaic (PV) Module safety Qualification-Part 2: Requirements for Testing. CENELEC: Brussels, Belgium, 2018.
37. IEC 62109-1; Safety of Power Converters for Use in Photovoltaic Power Systems—Part 1: General Requirements. CENELEC: Brussels, Belgium, 2010.

38. IEC 62109-2; Safety of power Converters for Use in Photovoltaic Power Systems-Part 2: Particular Requirements for Inverters. CENELEC: Brussels, Belgium, 2011.
39. Wang, G.; Wang, F.; Magai, G.; Lei, Y.; Huang, A.; Das, M. Performance comparison of 1200V 100A SiC MOSFET and 1200V 100A silicon IGBT. In Proceedings of the 2013 IEEE Energy Conversion Congress and Exposition, Denver, CO, USA, 15–19 September 2013. [CrossRef]
40. Datasheet of the Transistor C2M0080170P. Available online: <https://cms.wolfspeed.com/app/uploads/2020/12/C2M0080170P.pdf> (accessed on 9 October 2021).
41. Erickson, R.; Maksimovic, D. *Fundamentals of Power Electronics, Ser. Power Electronics*; Springer: Berlin/Heidelberg, Germany, 2001.
42. Datasheet of the diode C5D25170H. Available online: <https://cms.wolfspeed.com/app/uploads/2020/12/C5D25170H.pdf> (accessed on 9 October 2021).
43. Jain, S.; Agarwal, V. A Single-Stage Grid-Connected Inverter Topology for Solar PV Systems with Maximum Power Point Tracking. *IEEE Trans. Power Electron.* **2007**, *22*, 1928–1940. [CrossRef]
44. Altin, N.; Ozdemir, S.; Komurcugil, H.; Sefa, I.; Biricik, S. Two-stage grid-connected inverter for PV systems. In Proceedings of the 2018 IEEE 12th International Conference on Compatibility, Power Electronics and Power Engineering, Doha, Qatar, 10–12 April 2018. [CrossRef]
45. Zebarjadi, M.; Askarzadeh, A. Optimization of a reliable grid-connected PV-based power plant with/without energy storage system by a heuristic approach. *Sol. Energy* **2016**, *125*, 12–21. [CrossRef]
46. Xiao, W.; El Moursi, M.S.; Khan, O.; Infield, D. Review of grid-tied converter topologies used in photovoltaic systems. *IET Renew. Power Gener.* **2016**, *10*, 1543–1551. [CrossRef]
47. Zhang, Y.; Sen, P.C. A new soft-switching technique for buck, boost, and buck~boost converters. *IEEE Trans. Ind. Appl.* **2003**, *39*, 1775–1782. [CrossRef]
48. Verbytskyi, I.; Bondarenko, O.; Liivik, E. Control features of multi cell-type current regulator for resistance welding. In Proceedings of the 2017 IEEE 58th International Scientific Conference on Power and Electrical Engineering of Riga Technical University (RTUCON), Doha, Qatar, 10–12 April 2018. [CrossRef]
49. Jyotheeswara Reddy, K.; Sudhakar, N. High Voltage Gain Interleaved Boost Converter With Neural Network Based MPPT Controller for Fuel Cell Based Electric Vehicle Applications. *IEEE Access* **2018**, *6*, 3899–3908. [CrossRef]
50. Zeb, K.; Uddin, W.; Khan, M.A.; Ali, Z.; Ali, M.U.; Christofides, N.; Kim, H.J. A comprehensive review on inverter topologies and control strategies for grid connected photovoltaic system. *Renew. Sustain. Energy Rev.* **2018**, *94*, 1120–1141. [CrossRef]
51. Keyhani, H.; Toliyat, H.A. Single-Stage Multi string PV Inverter With an Isolated High-Frequency Link and Soft-Switching Operation. *IEEE Trans. Power Electron.* **2014**, *29*, 3919–3929. [CrossRef]
52. Khodabandeh, M.; Afshari, E.; Amirabadi, M. A Single-Stage Soft-Switching High-Frequency AC-Link PV Inverter: Design, Analysis, and Evaluation of Si-based and SiC-based Prototypes. *IEEE Trans. Power Electron.* **2018**, *34*, 2312–2326. [CrossRef]
53. Lopez, O.; Freijedo, F.D.; Yepes, A.G.; Fernandez-Comesana, P.; Malvar, J.; Teodorescu, R.; Doval-Gandoy, J. Eliminating ground current in a transformerless photovoltaic application. *IEEE Trans. Energy Convers.* **2010**, *25*, 140–147. [CrossRef]
54. Xiao, H.; Xie, S. Leakage current analytical model and application in single-phase transformerless photovoltaic grid-connected inverter. *IEEE Trans. Electromagn Compat.* **2010**, *52*, 902–913. [CrossRef]
55. Zhang, L.; Sun, K.; Xing, Y.; Xing, M. H6 Transformerless Full-Bridge PV Grid-Tied Inverters. *IEEE Trans. Power Electron.* **2014**, *29*, 1229–1238. [CrossRef]
56. Ahmed, M.H.; Wang, M.; Hassan, M.A.S.; Ullah, I. Power Loss Model and Efficiency Analysis of Three-phase Inverter Based on SiC MOSFETs for PV Applications. *IEEE Access* **2019**, *7*, 75768–75781. [CrossRef]
57. Escobar, G.; Martinez-Rodriguez, P.R.; Pool, E.I.; Pena-Quintal, A.E.; Vazquez, G.; Sosa, J.M. A model-based controller of a three-level stacked-cell grid connected converter. In Proceedings of the IECON 2015-41st Annual Conference of the IEEE Industrial Electronics Society, Yokohama, Japan, 9–12 November 2015. [CrossRef]
58. Mamadaminov, U.M. *Advanced Inverters and Their Functionalities for Distributed Solar Generation*; Energy Engineering III, Spring; Oregon Institute of Technology: Wilsonville, OR, USA, 2014.
59. Hidalgo, R.; Abbey, C. Integrating distributed generation with Smart Grid enabling technologies. In Proceedings of the IEEE PES Conference on Innovative Smart Grid Technologies Latin America SGT LA, Medellin, Colombia, 19–21 October 2011. [CrossRef]
60. Talha, M.; Amir, A.; Raihan, S.R.S.; Abd Rahim, N. Grid-connected photovoltaic inverters with low-voltage ride through for a residential-scale system: A review. *Int. Trans. Electr. Energy Syst.* **2020**, *31*, e12630. [CrossRef]
61. Taul, M.G.; Wang, X.; Davari, P.; Blaabjerg, F. An Overview of Assessment Methods for Synchronization Stability of Grid-Connected Converters Under Severe Symmetrical Grid Faults. *IEEE Trans. Power Electron.* **2019**, *34*, 9655–9670. [CrossRef]
62. Geddada, N.; Karanki, S.B.; Mishra, M.K. Synchronous reference frame based current controller with SPWM switching strategy for DSTATCOM applications. In Proceedings of the 2012 IEEE International Conference on Power Electronics, Drives and Energy Systems (PEDES), Bengaluru, India, 16–19 December 2012. [CrossRef]
63. Chappa, H.; Thakur, T. Voltage instability detection using synchrophasor measurements: A review. *Int. Trans. Electr. Energy Syst.* **2020**, *30*, 12343. [CrossRef]
64. Calleja, H.; Jimenez, H. Performance of a grid connected PV system used as active filter. *Energy Convers. Manag.* **2004**, *45*, 2417–2428. [CrossRef]

65. Verbytskyi, Y.V. Double Fourier series using for calculating modulating signals spectrum. *Tekhnichna Elektrodynamika* **2014**, *4*, 96–98.
66. Adewuyi, O.B.; Shigenobu, R.; Ooya, K.; Senjyu, T.; Howlader, A.M. Static voltage stability improvement with battery energy storage considering optimal control of active and reactive power injection. *Electr. Power Syst. Res.* **2019**, *172*, 303–312. [[CrossRef](#)]
67. Pinnangudi, B.; Kuykendal, M.; Bhadra, S. Smart Grid Energy Storage. *Power Grid* **2017**, 93–135. [[CrossRef](#)]
68. Liu, S.; Xie, X.; Yang, L. Analysis, Modeling and Implementation of a Switching Bi-directional Buck-Boost Converter Based on Electric Vehicle Hybrid Energy Storage for V2G System. *IEEE Access* **2020**, *8*, 65868–65879. [[CrossRef](#)]
69. Pakkiraiah, B.; Sukumar, G.D. Research Survey on Various MPPT Performance Issues to Improve the Solar PV System Efficiency. *J. Sol. Energy* **2016**, *2016*, 8012432. [[CrossRef](#)]
70. Yang, J.-H.; Jeong, K.-I.; Kwon, J.-M. Energy storage system with PV generation and online UPS functions. In Proceedings of the 2014 IEEE 36th International Telecommunications Energy Conference (INTELEC), Vancouver, BC, Canada, 28 September–2 October 2014. [[CrossRef](#)]
71. Li, K.; Zhao, J.; Ma, Q.; Xu, H. Hierarchy control of power quality for wind–battery energy storage system. *IET Power Electron.* **2014**, *7*, 2123–2132. [[CrossRef](#)]
72. Li, X.; Wang, S. A review on energy management, operation control and application methods for grid battery energy storage systems. *CSEE J. Power Energy Syst.* **2019**, *7*, 1026–1040. [[CrossRef](#)]
73. Hannan, M.A.; Hoque, M.M.; Hussain, A.; Yusof, Y.; Ker, P.J. State-of-the-Art and Energy Management System of Lithium-Ion Batteries in Electric Vehicle Applications: Issues and Recommendations. *IEEE Access* **2018**, *6*, 19362–19378. [[CrossRef](#)]
74. Ortúzar, M.; Dixon, J.; Moreno, J. Ultracapacitor-Based Auxiliary Energy System for an Electric Vehicle: Implementation and Evaluation. *IEEE Trans. Ind. Electron.* **2007**, *54*, 2147–2156. [[CrossRef](#)]
75. Fernandez, G. A Bidirectional Buffered Charging Unit for EV's (BBCU). In Proceedings of the International Power Electronics Conference (IPEC-Niigata 2018-ECCE Asia), Niigata, Japan, 20–24 May 2018. [[CrossRef](#)]
76. Schupbachj, R.M.; Bald, C. Comparing DC-DC Converters for Power Management in Hybrid Electric Vehicles. In Proceedings of the IEEE International Electric Machines and Drives Conference, Madison, WI, USA, 1–4 June 2003; Volume 3, pp. 1369–1374. [[CrossRef](#)]
77. Czogalla, J.; Li, J.; Sullivan, C.R. Automotive Application of Multi-Phase Coupled-Inductor DC-DC Converter. In Proceedings of the IEEE Industry Applications Conference, Salt Lake City, UT, USA, 12–16 October 2003; Volume 3, pp. 1524–1529. [[CrossRef](#)]
78. Farhangi, B.; Toliyat, H.A. Modeling and Analyzing Multiport Isolation Transformer Capacitive Components for Onboard Vehicular Power Conditioners. *IEEE Trans. Ind. Electron.* **2015**, *62*, 3134–3142. [[CrossRef](#)]
79. Inoue, S.; Akagi, H. A Bi-Directional DC/DC Converter for an Energy Storage System. In Proceedings of the APEC 07-Twenty-Second Annual IEEE Applied Power Electronics Conference and Exposition, Anaheim, CA, USA, 25 February–1 March 2007. [[CrossRef](#)]
80. Xu, X.; Khambadkone, A.M.; Oruganti, R. A Soft-Switched Back-to-Back Bi-directional DC/DC Converter with an FPGA based Digital Control for Automotive applications. In Proceedings of the IECON 2007-33rd Annual Conference of the IEEE Industrial Electronics Society, Taipei, Taiwan, 5–8 November 2007. [[CrossRef](#)]
81. Jang, S.-J.; Lee, T.W.; Lee, W.C.; Won, C.Y. Bidirectional DC to DC Converters for Fuel Cell Generation System. *Power Electron. Spec. Conf.* **2004**, *6*, 4722–4728. [[CrossRef](#)]
82. Lin, B.R.; Hung, T.L. Single-phase half-bridge converter topology for power quality compensation. *Electr. Power Appl. IEE Proc.* **2002**, *149*, 351–359. [[CrossRef](#)]
83. Lin, B.R.; Hung, T.L.; Huang, C.H. Bi-directional single-phase half-bridge rectifier for power quality compensation. *Electr. Power Appl. IEE Proc.* **2003**, *150*, 397–406. [[CrossRef](#)]
84. Korkh, O.; Blinov, A.; Vinnikov, D. Analysis of Oscillation Suppression Methods in the AC-AC Stage of High Frequency Link Converters. In Proceedings of the IEEE 60th International Scientific Conference on Power and Electrical Engineering of Riga Technical University (RTUCON), Riga, Latvia, 7–9 October 2019. [[CrossRef](#)]
85. Bilgin, B.; Emadi, A.; Krishnamurthy, M. Universal input battery charger circuit for PHEV applications with the simplified controller. In Proceedings of the Applied Power Electronics Conference and Exposition (APEC), Fort Worth, TX, USA, 6–11 March 2011; pp. 815–820. [[CrossRef](#)]
86. Segaran, D.; Holmes, D.G.; McGrath, B.P. High performance bi-directional AC-DC converters for PHEV with minimized DC bus capacitance. In Proceedings of the IECON 37th Annual Conference on IEEE Industrial Electronics Society, Melbourne, Australia, 7–10 November 2011; pp. 3620–3625. [[CrossRef](#)]
87. Odamov, U.O.; Kamilov, M.M.; Niyazov, S.K.; Song, K. Research of the efficiency of the solar battery operations in real exploitation conditions. *Sci. Rep. Bukhara State Univ.* **2021**, *5*, 2–17. [[CrossRef](#)]
88. Saidi, A.S.; Slimene, M.B.; Khelifi, M.A. Transient stability analysis of photovoltaic system with experimental shading effects. *Eng. Technol. Appl. Sci. Res.* **2018**, *8*, 3592–3597. [[CrossRef](#)]
89. Araujo, S.V.; Torricco-Bascope, R.P.; Torricco-Bascope, G.V.; Menezes, L. Step-up converter with high voltage gain employing three-state switching cell and voltage multiplier. In Proceedings of the 2008 IEEE Power Electronics Specialists Conference, Rhodes, Greece, 15–19 June 2008; pp. 2271–2277. [[CrossRef](#)]

90. Ahmad, J.; Pervez, I.; Sarwar, A.; Tariq, M.; Fahad, M.; Chakraborty, R.K.; Ryan, M.J. Performance Analysis and Hardware-in-the-Loop (HIL) Validation of Single Switch High Voltage Gain DC-DC Converters for MPP Tracking in Solar PV System. *IEEE Access* **2021**, *9*, 48811–48830. [[CrossRef](#)]
91. Arunkumari, T.; Indragandhi, V. An overview of high voltage conversion ratio DC-DC converter configurations used in DC micro-grid architectures. *Renew. Sustain. Energy Rev.* **2017**, *77*, 670–687. [[CrossRef](#)]
92. Blinov, A.; Verbytskyi, I.; Zinchenko, D.; Vinnikov, D.; Galkin, I. Modular Battery Charger for Light Electric Vehicles. *Energies* **2020**, *13*, 774. [[CrossRef](#)]
93. Norrga, S. Experimental Study of a Soft-Switched Isolated Bidirectional AC DC Converter Without Auxiliary Circuit. *IEEE Trans. Power Electron.* **2006**, *21*, 1580–1587. [[CrossRef](#)]
94. Kummari, N.; Chakraborty, S.; Chattopadhyay, S. An Isolated High-Frequency Link Microinverter Operated with Secondary-Side Modulation for Efficiency Improvement. *IEEE Trans. Power Electron.* **2018**, *33*, 2187–2200. [[CrossRef](#)]
95. Nayak, P.; Rajashekar, K.; Pramanick, S. Soft-Switched Modulation Technique for a Single-Stage Matrix-Type Isolated DC-AC Converter. *IEEE Trans. Ind. Appl.* **2019**, *55*, 7642–7656. [[CrossRef](#)]
96. Tibola, G.; Lemmen, E.; Duarte, J.L.; Barbi, I. Passive Regenerative and Dissipative Snubber Cells for Isolated SEPIC Converters: Analysis, Design, and Comparison. *IEEE Trans. Power Electron.* **2017**, *32*, 9210–9222. [[CrossRef](#)]
97. Blinov, A.; Verbytskyi, I.; Peftitsis, D.; Vinnikov, D. Regenerative Passive Snubber Circuit for High-Frequency Link Converters. *IEEE J. Emerg. Sel. Top. Ind. Electron.* **2021**, *3*, 252–257. [[CrossRef](#)]
98. Blinov, A.; Kosenko, R.; Chub, A.; Vinnikov, D. Snubberless boost full-bridge converters: Analysis of soft-switching performance and limitations. *Int. J. Circ. Theor. Appl.* **2019**, *47*, 884–908. [[CrossRef](#)]
99. Luo, F.L.; Ye, H. Positive output super-lift converters. *IEEE Trans. Power Electron.* **2003**, *18*, 105–113. [[CrossRef](#)]
100. Zhang, S.; Xu, J.; Yang, P. A single-switch high gain quadratic boost converter based on voltage-lift technique. In Proceedings of the 10th International Power & Energy Conference (IPEC), Ho Chi Minh City, Vietnam, 12–14 December 2012; pp. 71–75. [[CrossRef](#)]
101. Axelrod, B.; Berkovich, Y.; Shenkman, A.; Golan, G. Diode-capacitor voltage multipliers combined with boost-converters: Topologies and characteristics. *IET Power Electron.* **2012**, *5*, 873–884. [[CrossRef](#)]
102. Wu, G.; Ruan, X.; Ye, Z. Nonisolated High Step-Up DC-DC Converters Adopting Switched-Capacitor Cell. *IEEE Trans. Ind. Electron.* **2015**, *62*, 383–393. [[CrossRef](#)]
103. Tofoli, F.L.; de Souza Oliveira, D.; Torrico-Bascopé, R.P.; Alcazar, Y.J.A. Novel Nonisolated High-Voltage Gain DC-DC Converters Based on 3SSC and VMC. *IEEE Trans. Power Electron.* **2012**, *27*, 3897–3907. [[CrossRef](#)]
104. Zhang, J.; Huang, L.; Shu, J.; Wang, H.; Ding, J. Energy Management of PV-diesel-battery Hybrid Power System for Island Stand-alone Micro-grid. *Energy Procedia* **2017**, *105*, 2201–2206. [[CrossRef](#)]
105. Cano, A.; Jurado, F.; Sánchez, H.; Fernández, L.M.; Castañeda, M. Optimal sizing of stand-alone hybrid systems based on PV/WT/FC by using several methodologies. *J. Energy Inst.* **2014**, *87*, 330–340. [[CrossRef](#)]
106. Ghaffari, A.; Askarzadeh, A. Design optimization of a hybrid system subject to reliability level and renewable energy penetration. *Energy* **2020**, *193*, 116754. [[CrossRef](#)]
107. Noshahr, J.B.; Mohamadi, B.; Kermani, M.; Kermani, M. Operational Planning of Inverter Control in a grid-connected Microgrid with hybrid PV and BESS. In Proceedings of the 2020 IEEE International Conference on Environment and Electrical Engineering and 2020 IEEE Industrial and Commercial Power Systems Europe (EEEIC/I & CPS Europe), Madrid, Spain, 9–12 June 2020. [[CrossRef](#)]
108. Vahid, S.; EL-Refaie, A. A Novel Topology for an Extendable Isolated DC-DC Multi-port Power Converter with a Multipurpose Hybrid Energy Storage System. In Proceedings of the 2020 IEEE Energy Conversion Congress and Exposition (ECCE), Detroit, MI, USA, 11–15 October 2020. [[CrossRef](#)]
109. Pereira, T.; Hoffmann, F.; Zhu, R.; Liserre, M. A Comprehensive Assessment of Multiwinding Transformer-Based DC-DC Converters. *IEEE Trans. Power Electron.* **2021**, *36*, 10020–10036. [[CrossRef](#)]
110. Wu, H.; Xing, Y.; Xia, Y.; Sun, K. A family of non-isolated three-port converters for stand-alone renewable power systems. In Proceedings of the IECON 2011-37th Annual Conference of the IEEE Industrial Electronics Society, Melbourne, Australia, 7–10 November 2011. [[CrossRef](#)]
111. Zhang, M.; Xing, Y.; Wu, H.; Lu, Y.; Sun, K. Performance evaluation of a non-isolated bidirectional three-port power converter for energy storage applications. In Proceedings of the 2016 IEEE 8th International Power Electronics and Motion Control Conference (IPEMC-ECCE Asia), Hefei, China, 22–26 May 2016; pp. 2703–2708. [[CrossRef](#)]
112. Sato, Y.; Uno, M.; Nagata, H. Nonisolated Multiport Converters Based on Integration of PWM Converter and Phase-Shift Switched-Capacitor Converter. *IEEE Trans. Power Electron.* **2019**, *35*, 455–470. [[CrossRef](#)]
113. Faraji, R.; Farzanehfard, H. Fully Soft Switched Multi-Port DC-DC Converter with High Integration. *IEEE Trans. Power Electron.* **2020**, *36*, 1901–1908. [[CrossRef](#)]
114. Kwasinski, A. Identification of Feasible Topologies for Multiple-Input DC-DC Converters. *IEEE Trans. Power Electron.* **2009**, *24*, 856–861. [[CrossRef](#)]
115. Balaji, C.; Chellammal, N.; Sanjeevikumar, P.; Bhaskar, M.S.; Holm-Nielsen, J.B.; Leonowicz, Z.; Masebinu, S.O. Non-Isolated High-Gain Triple Port DC-DC Buck-Boost Converter with Positive Output Voltage for Photovoltaic Application. *IEEE Access* **2020**, *2020*, 3003192. [[CrossRef](#)]

116. Thang, T.V.; Ahmed, A.; Kim, C.I.; Park, J.H. The flexible system architecture of stand-alone PV power generation with the energy storage device. *IEEE Trans. Energy Convers.* **2015**, *30*, 1386–1396. [[CrossRef](#)]
117. Amirabadi, M.; Toliyat, H.A.; Alexander, W.C. A multiport ac link PV inverter with reduced size and weight for a stand-alone application. *IEEE Trans. Ind. Appl.* **2013**, *49*, 2217–2228. [[CrossRef](#)]
118. Hassan, S.Z.; Mumtaz, S.; Kamal, T.; Khan, L. Performance of grid-integrated photovoltaic/fuel cell/ electrolyzer/battery hybrid power system. In Proceedings of the 2015 Power Generation Systems and Renewable Energy Technologies, PGSRET, Islamabad, Pakistan, 10–11 June 2015. [[CrossRef](#)]
119. Jayasinghe, S.D.; Vilathgamuwa, D.M.; Madawala, U.K. Diodeclamped three-level inverter-based battery/supercapacitor direct integration scheme for renewable energy systems. *IEEE Trans. Power Electron.* **2011**, *26*, 3720–3729. [[CrossRef](#)]
120. Rangu, S.K.; Lolla, P.R.; Dhenuvakonda, K.R.; Singh, A.R. Recent trends in power management strategies for optimal operation of distributed energy resources in microgrids: A comprehensive review. *Int. J. Energy Res.* **2020**, *44*, 9889–9911. [[CrossRef](#)]
121. David, F. *Probability and Statistics for Computer Science*; Springer International Publishing: Berlin/Heidelberg, Germany, 2018; p. 367. [[CrossRef](#)]